THE ASTROPHYSICAL JOURNAL, 502:199–217, 1998 July 20

HUBBLE SPACE TELESCOPE AND VLA OBSERVATIONS OF SEYFERT 2 GALAXIES: THE RELATIONSHIP BETWEEN RADIO EJECTA AND THE NARROW-LINE REGION[1]

HEINO FALCKE[2] AND ANDREW S. WILSON[3]
Astronomy Department, University of Maryland, College Park, MD 20742-2421; wilson@astro.umd.edu
AND
CHRIS SIMPSON
Jet Propulsion Laboratory, MS 169-327, 4800 Oak Grove Drive, Pasadena, CA 91109; bart@fornax.jpl.nasa.gov
Received 1997 September 11; accepted 1998 January 12

ABSTRACT

We present *HST*/WFPC2 images, in narrowband filters containing the [O III] λ5007 and Hα + [N II] emission lines and their adjacent continua, of a sample of seven Seyfert 2 galaxies selected because they possess either extended emission-line regions in ground-based observations or a hidden broad-line region in polarized light. Six of the galaxies have also been observed with the VLA in order to obtain radio maps of better quality and angular resolution than those in the literature. We find detailed correspondences between features in the radio and emission-line images, clearly indicating strong interactions between the radio jets and the interstellar medium. Such interactions play a major role in determining the morphology of the NLR, as the radio jets sweep up and compress ambient gas, producing ordered structures with enhanced surface brightness in line emission. In at least three galaxies, namely, Mrk 573, ESO 428-G14, and Mrk 34 (and perhaps also NGC 7212), off-nuclear radio lobes coincide with regions of low gaseous excitation (as measured by the [O III]/(Hα + [N II]) ratio). In Mrk 573 and NGC 4388, there is a clear trend for low-brightness ionized gas to be of higher excitation. These results may be understood if radio lobes and regions of high emission-line surface brightness are associated with high gas densities, reducing the ionization parameter. [O III]/(Hα + [N II]) excitation maps reveal bipolar structures that can be interpreted as either the ionization cones expected in the unified scheme or widening, self-excited gaseous outflows. Only NGC 4388 and Mrk 573 show a clearly defined, straight-edged ionization cone.

Subject headings: galaxies: Seyfert — galaxies: structure — radio continuum: galaxies

1. INTRODUCTION

The strong tendency for the circumnuclear emission-line and radio morphologies to be aligned in Seyfert galaxies (e.g., Unger et al. 1987; Pogge 1988; Haniff, Wilson, & Ward 1988) added weight to the idea that the ionizing radiation escapes preferentially from the active nucleus along the radio axis. When some of these structures were revealed to be well-defined cones by virtue of the improved resolution offered by the *Hubble Space Telescope* (*HST*; e.g., NGC 1068, Evans et al. 1991; NGC 5728, Wilson et al. 1993; NGC 5643, Simpson et al. 1997), the anisotropic escape of ionizing photons was confirmed. This effect is most popularly explained by the presence of an optically thick "obscuring torus" (Antonucci 1993), which is able to collimate the intrinsically isotropic ionizing radiation (see, e.g., Storchi-Bergmann, Mulchaey, & Wilson 1993). In addition, a number of galaxies display an "ionization cone" morphology when an excitation map is made, e.g., in [O III]/(Hα + [N II]).

The close connection between the radio ejecta of Seyfert nuclei and their narrow-line regions (NLRs) initially became apparent from their similar spatial extents and from strong correlations between radio luminosities and [O III] λ5007 luminosity and line width (de Bruyn & Wilson 1978; Wilson & Willis 1980; Whittle 1985, 1992). Spectroscopic studies of the NLR (Baldwin, Wilson, & Whittle 1987; Whittle et al. 1988) have revealed that the kinematics of the gas are often clearly affected by the radio jets. Such interactions could play a role in determining the structure of the NLR within the region ionized by the nucleus. In a handful of cases, *HST* has shown a clear spatial correspondence between the radio and emission-line distributions (e.g., NGC 5929, Bower et al. 1994; Mrk 78, Capetti et al. 1994, 1996; Mrk 1066, Bower et al. 1995; Mrk 3, Capetti et al. 1996; ESO 428-G14, Falcke et al. 1996b), indicating that the radio ejecta strongly perturb the ionized gas, at least in these objects. It has also been suggested that the hot gas associated with the shocks generated by the interaction between the radio ejecta and the ambient medium is a significant source of ionizing radiation (e.g., Dopita 1995; Dopita & Sutherland 1995; Bicknell et al. 1998; see also reviews in Morse, Raymond, & Wilson 1996 and Wilson 1996).

It is therefore of great importance to study more Seyfert galaxies at the high spatial resolution that only *HST* can provide, to determine whether the morphology of the narrow-line region is determined by the nuclear ionizing radiation or by the interaction of radio jets with the interstellar medium, or by a combination of both. In this paper we present images of seven Seyfert 2 galaxies, selected because they possess either extended emission-line regions (as seen in ground-based images) or broad lines in polarized

[1] Based on observations with the NASA/ESA *Hubble Space Telescope*, obtained at the Space Telescope Science Institute, which is operated by AURA, Inc., under NASA contract NAS 5-26555, and on observations made with the VLA operated by NRAO.

[2] Current Address: Max-Planck-Institut für Radioastronomie, Auf dem Hügel 69, D-53121 Bonn, Germany; hfalcke@mpifr-bonn.mpg.de.

[3] Adjunct astronomer, Space Telescope Science Institute.

light, taken with the Wide Field and Planetary Camera 2 (WFPC2). For each galaxy, we have images in the light of the [O III] λ5007 line and the Hα + [N II] $\lambda\lambda$6548, 6583 blend, as well as in adjacent continua. We also present new radio maps taken with the Very Large Array (VLA), almost all in A configuration, providing an angular resolution comparable to that of the *HST* images. Taken together, these allow us to directly compare the structures of the line-emitting gas and radio plasma on scales of tens of parsecs.

We give the details of our observations in § 2. The results are presented on a galaxy-by-galaxy basis in § 3, and in § 4 we discuss these results and their implications for the role of the radio jets in shaping the narrow-line region. Some concluding remarks are given in § 5. Throughout this paper we adopt a Hubble constant of $H_0 = 75\ \mathrm{km\ s^{-1}\ Mpc^{-1}}$.

2. OBSERVATIONS AND DATA REDUCTION

2.1. *HST Observations*

All galaxies in our sample were observed with the WFPC2 on board *HST*. Except for observations of Hα + [N II] and the red continuum of ESO 428-G14, we used the linear ramp filters (LRFs) of the WFPC2, which have position-dependent wavelengths of peak transmission, to image objects in their redshifted emission lines and their adjacent continua. This means that in order to observe a galaxy at a specific wavelength with the LRFs, the object had to be placed at a specific position within the field of view (FOV) of the WFPC2. In most cases, the image will therefore not be taken with the Planetary Camera (PC) but rather with one of the three chips of the Wide Field Camera (WF). The former has a higher resolution, with 0.″0455 pixel^{-1}, while the latter have 0.″1 pixel^{-1}. The transmissions and passbands of the LRFs are also position dependent; the transmission ranges between 40% and 80% and the passband is $\Delta\lambda/\lambda \sim 1.3\%$, with a roughly triangular or Gaussian transmission profile. The passband and the run of the central wavelength with position translate into an upper limit of 14″ for the size of an emission-line region that can be imaged with the LRFs.

For our observations, the filters and central wavelengths were chosen such that they were centered on the redshifted Hα (6563 Å) and [O III] 5007 Å (hereafter referred to simply as [O III]) emission lines and their adjacent continua, all observations being split into two integrations to allow cosmic ray rejection. Due to the relatively large filter width, the [N II] $\lambda\lambda$6548, 6583 contribution to the Hα images is significant (typically between a third and one-half), depending on the local [N II]/Hα ratio and the position on the chip.

The details of the observations are given in Table 1. All exposures were bias- and dark-subtracted by WFPC2 pipeline processing at the Space Telescope Science Institute. Since flat fields were not available for the LRFs, we used flat fields taken in nearby narrowband filters (F502N and F673N). The exposures were then combined to remove cosmic rays and corrected for geometric distortions, since line and continuum images were in general taken at different positions on the chip. The images were then rotated to the cardinal orientation (north up, east to the left).

The continuum images were subtracted from the line images by shifting them to a common reference frame according to the coordinate information in the image headers. Usually, each of the on- and off-band pairs were

TABLE 1

HST OBSERVATION LOG

Galaxy (1)	z (2)	Filter (3)	λ_c (4)	Chip (5)	Exposure (6)	Date (7)	File Name (8)	ID (9)
Mrk 348	0.01514	FR533N	5080	WF2	300.00	1995 Dec 16	U2XI0601(2)T	[O III] λ5007
(NGC 262)		FR533P15	5330	WF4	140.00		U2XI0603(4)T	[O III] cont.
		FR680N	6666	WF2	300.00		U2XI0605(6)T	Hα + [N II]
		FR680N	6580	WF3	140.00		U2XI0607(8)T	Hα + [N II] cont.
Mrk 573	0.0173	FR533N	5092	WF2	300.00	1995 Nov 12	U2XI0701(2)T	[O III] λ5007
(UGC01214)		FR533N	5345	WF4	140.00		U2XI0703(4)T	[O III] cont.
		FR680N	6679	WF2	300.00		U2XI0705(6)T	Hα + [N II]
		FR680N	6514	WF3	140.00		U2XI0707(8)T	Hα + [N II] cont.
ESO 428-G14	0.00544	FR533N	5034	WF2	140.00	1996 Jan 14	U2XI0301(2)T	[O III] λ5007
		FR533N	5284	WF3	140.00		U2XI0303(4)T	[O III] cont.
		F658N	6590	PC1	400.00	1995 Apr 17	U2NP0601(2)T	Hα + [N II]
		F814W	7940	PC1	100.00		U2NP0603(4)T	Hα + [N II] cont.
Mrk 1210	0.0135	FR533N	5068	WF2	140.00	1995 Nov 24	U2XI0501(2)T	[O III] λ5007
(UGC04203)		FR533P15	5319	WF4	140.00		U2XI0503(4)T	[O III] cont.
		FR680N	6654	WF2	350.00		U2XI0505(6)T	Hα + [N II]
		FR680N	6551	WF3	140.00		U2XI0507(8)T	Hα + [N II] cont.
Mrk 34	0.0505	FR533	5263	WF3	230.00	1995 Nov 08	U2XI0101(2)T	[O III] λ5007
		FR533N18	5499	WF3	160.00		U2XI0103(4)T	[O III] cont.
		FR680N18	6900	WF2	140.00		U2XI0105(6)T	Hα + [N II]
		FR680N	6727	WF2	140.00		U2XI0107(8)T	Hα + [N II] cont.
NGC 4388	0.00842	FR533N	5053	WF2	140.00	1996 Mar 27	U2XI0201(2)T	[O III] λ5007
		FR533N	5304	WF3	140.00		U2XI0203(4)T	[O III] cont.
		FR680P15	6614	PC1	350.00		U2XI0205(6)T	Hα + [N II]
		FR680P	6448	WF3	140.00		U2XI0207(8)T	Hα + [N II] cont.
NGC 7212	0.0266	FR533N	5136	WF2	300.00	1995 Sep 26	U2XI0401(2)T	[O III] λ5007
		FR533N	5388	WF4	140.00		U2XI0403(4)T	[O III] cont.
		FR680N	6734	WF2	346.50		U2XI0405(6)T	Hα + [N II]
		FR680N	6567	WF3	140.00		U2XI0407(8)T	Hα + [N II] cont.

NOTE—Columns: (1) galaxy; (2) redshift; (3) filter name; (4) central wavelength in Å; (5) WFPC2 chip; (6) exposure time of each exposure in s (total exposure time of each image is twice that value); (7) observation date; (8) root file name(s) of the two (CR-split) exposures per image; (9) identification for this paper.

taken during the same orbit with guide stars in fine lock, so the relative astrometry should be better than 20 mas. However, since all our observations were interrupted by earth occultations, we could not rely in all cases solely on the spacecraft information to align the [O III] and Hα + [N II] images of each galaxy. We therefore aligned the green and red images according to their continuum peaks and checked the results by cross-correlating bright features in the emission-line images. With this method we achieved subpixel (i.e., $\sim$0.5 pixel) precision in all cases for the relative alignment of the continuum-subtracted emission-line images. This additional step is essential in order to avoid artifacts in the excitation maps.

2.2. *VLA Observations*

In order to compare the *HST* images with radio maps of similar resolution, we have obtained new radio observations with the VLA for all galaxies in our sample except Mrk 348, which has a known VLBI core (Neff & de Bruyn 1983). All galaxies were observed at the X band (3.5 cm) in A configuration, except for NGC 4388, which was observed in BnA configuration. In addition, *U*-band (2 cm) observations were obtained for Mrk 573 and ESO 428-G14, and C-band (6.1 cm) observations were obtained for Mrk 34. The best resolutions achieved were 0.″14, 0.″24, and 0.″35 at 2, 3.5, and 6.1 cm, respectively. For scheduling reasons, two of the sources (NGC 7212 and Mrk 1210) were observed in snapshot mode only. The details of these observations are given in Table 2.

Weather conditions were excellent for all observations. Integrations on the galaxies were sandwiched between observations of a calibrator with typical on-galaxy integrations of 8 and 12 minutes at 2 cm and 3.5 cm, respectively. Data reduction was done in Socorro with AIPS following standard procedures with very little flagging of bad data points being necessary. The phases of the calibrators were interpolated and applied to the program objects; 3C286 was used as the primary flux calibrator. Maps of the galaxies were produced using the AIPS task IMAGR with various beam sizes, cleaning depths of several thousand iterations, a CLEAN gain factor of 0.1, uniform weighting for high-resolution maps, and natural weighting for low-resolution maps.

2.3. *Radio and Optical Registration*

Since absolute positions derived from *HST* observations have an error on the order of 1″, the registration between the radio and the optical frames is a critical issue. Meaningful registration cannot, therefore, rely on the internal *HST* astrometry, and one must shift the *HST* images to align with the radio. Unfortunately, with the exception of NGC 4388 and NGC 7212 (see below), ground-based astrometric measurements are not yet available for stars in the WFPC2 frames, so we have used the following procedure for aligning the images. First, we smoothed the red-continuum *HST* image to a resolution of 1.″5 (FWHM), thus simulating a ground-based, seeing-limited image. The red continuum was chosen because it generally has a higher signal-to-noise ratio (S/N), and we did not find significant offsets between the green and red peaks. We then determined the peak in the smoothed *HST* image, assigned to it the coordinates that were previously determined for those galaxies by ground-based astrometry (cols. [2] and [3] in Table 3), in most cases with a precision of tenths of an arcsecond; we then used this as the new coordinate system for the *HST* images. The resulting shifts of the *HST* coordinates varied between 0.″5 and 2″. With the exception of two galaxies (NGC 4388 and NGC 7212), the exact width of the Gaussian used for smoothing ("seeing") did not make a significant difference to the position of the peak in the smoothed *HST* image.

In columns (4) and (5) of Table 3, we give the positions of the continuum peaks of the unsmoothed *HST* image in the corrected (i.e., ground-based) coordinate frame. Comparison of columns (2) and (3) with columns (4) and (5) shows that in general the peaks in the smoothed and unsmoothed images (both measured in the same frame) agree with each other to better than 2 WF pixels (0.″2). For two objects (ESO 428-G14 and Mrk 1210), no subarcsecond accuracy positions are available yet, and we have listed the best available positions from the literature.

Even though NGC 4388 has astrometric positions of subarcsecond accuracy in the literature (Argyle & Eldridge 1990, hereafter AE90), we found this position to be useless for our purposes; because of the asymmetric brightness distribution of the *HST* continuum image of this galaxy, the position of the peak in the smoothed *HST* continuum image depends critically on the assumed width of the Gaussian smoothing function. We also found a large offset between the radio and the optical positions. For NGC 7212, we also observe a large offset between radio and the astrometric optical position (Clements 1983), and hence needed to check this registration as well.

R. W. Argyle (1997, private communication) kindly provided us with astrometric positions of two field stars visible

TABLE 2

VLA Observation Log

Galaxy	Configuration[a]	Band (cm)	Integration Time[b]	Phase Calibrator	Date
Mrk 573	A	2.0	3:20	0122−003	1996 Nov 04
	A	3.5	1:04	0122−003	1996 Nov 04
ESO 428-G14	A	2.0	2:56	0646−306	1996 Nov 04
	A	3.5	1:05	0646−306	1996 Nov 04
Mrk 1210	A	3.5	0:15	0745+100	1996 Nov 04
Mrk 34	A	3.5	2:42	1030+611	1996 Nov 04
	A	6.1	1:13	1030+611	1996 Nov 04
NGC 4388	BnA	3.5	1:11	1239+075	1997 Feb 01
NGC 7212	A	3.5	0:14	2144+092	1996 Nov 04

[a] VLA array configuration.

[b] Total integration time on source (hr:minute).

TABLE 3

OPTICAL AND RADIO POSITIONS

GALAXY (1)	OPTICAL POSITION J2000/B1950 R.A. (2)	Decl. (3)	*HST* NUCLEUS J2000/B1950 R.A. (4)	Decl. (5)	VLA NUCLEUS J2000/B1950 R.A. (6)	Decl. (7)
Mrk 348	00 48 47.128	+31 57 25.45[a]	00 48 47.130	+31 57 25.44	00 48 47.107	+31 57 25.32[b]
	00 46 04.882	+31 41 04.58	00 46 04.884	+31 41 04.57	00 46 04.861	+31 41 04.45
Mrk 573	01 43 57.772	+02 20 59.67[a]	01 43 57.771	+02 20 59.66	01 43 57.748	+02 20 59.58[c]
	01 41 22.922	+02 05 56.32	01 41 22.921	+02 05 56.30	01 41 22.898	+02 05 56.22
ESO 428-G14	07 16 31.2	−29 19 28[d]	07 16 31.2	−29 19 28	07 16 31.207	−29 19 28.89[c]
	07 14 32.9	−29 14 04	07 14 32.9	−29 14 04	07 14 32.930	−29 14 04.51
Mrk 1210	08 04 05.95	+05 06 50.4[e]	08 04 05.95	+05 06 50.4	08 04 05.841	+05 06 49.72[c]
	08 01 27.01	+05 15 22.0	08 01 27.01	+05 15 22.0	8 01 26.902	+05 15 21.32
Mrk 34	10 34 08.583	+60 01 51.74[a]	10 34 08.593	+60 01 51.62	10 34 08.568	+60 01 51.82[c]
	10 30 51.458	+60 17 21.84	10 30 51.468	+60 17 21.72	10 30 51.443	+60 17 21.92
NGC 4388	12 25 46.740	+12 39 42.05[f]	12 25 46.715	+12 39 43.41[f]	12 25 46.745	+12 39 43.51[g]
	12 23 14.635	+12 56 18.58	12 23 14.610	+12 56 19.94	12 23 14.640	+12 56 20.04
NGC 7212	22 07 02.006	+10 14 00.75[h]	22 07 01.998	+10 14 00.75	22 07 01.934	+10 14 01.01[c]
	22 04 33.976	+09 59 20.36	22 04 33.967	+09 59 20.37	22 04 33.903	+09 59 20.63

NOTE—Units of right ascension are hours, minutes, and seconds, and units of declination are degrees, arcminutes, and arcseconds. Cols. (2)–(3): R.A. and decl. of the optical nucleus as measured from the ground (upper is in J2000, lower in B1950). Cols. (4)–(5): R.A. and decl. of the red *HST* continuum peak from the ground-based astrometric positions given in Cols. (2) and (3) (see text). Cols. (6)–(7): R.A. and decl. of the VLA radio component identified as the nucleus. References for ground-based positions and uncertainties are noted below.

[a] Clements (1981); $\sigma_{\mathrm{R.A./decl}} \simeq 0\farcs15$.

[b] Ulvestad & Wilson (1984); $\sigma_{\mathrm{R.A./decl}} \simeq 0\farcs1$.

[c] This paper, with an error better than $0\farcs3$.

[d] Véron-Cetty & Véron (1996); $\sigma_{\mathrm{R.A./decl}} \simeq 2\farcs5$.

[e] Kojoian, Eliot, & Bicay (1981); $\sigma_{\mathrm{R.A./decl}} \simeq 1\farcs5$.

[f] Optical coordinates for the nucleus of this galaxy were derived from *HST* images registered by reference to a nearby field star ($12^{\mathrm{h}}25^{\mathrm{m}}49\fs869$, $+12°40'47\farcs95$ J2000) that happened to be visible in the *HST* FOV. The position of this star relative to the *Hipparcos* frame was provided by R. W. Argyle (1997, private communication) and is accurate to within $0\farcs1$ in R.A. and decl. The derived *HST* positions have errors of $\sigma_{\mathrm{R.A./decl}} \simeq 0\farcs2$.

[g] Position of the radio nucleus was taken from the VLA 2 cm A-configuration observations of Carral et al. (1990).

[h] Optical coordinates for the nucleus of this galaxy were derived similarly to those of NGC 4388; the reference field star was at (J2000) $22^{\mathrm{h}}06^{\mathrm{m}}58\fs240$, $10°15'05\farcs01$ (R. W. Argyle 1997, private communication), and the estimated errors of the *HST* positions are $\sigma_{\mathrm{R.A./decl}} \simeq 0\farcs2$.

in the *HST* images near NGC 4388 and NGC 7212, which we then used to assign an absolute coordinate system to the *HST* frames (see notes to Table 3). By comparing the positions of the same stars in our FOV in different exposures at different wavelengths (i.e., different positions in the LRF images), we find that the accuracy of those positions should be better than $\sim 0\farcs2$ across the FOV of the WFC.

Moreover, we found that our own position for the radio nucleus of NGC 4388 (which was observed with a very elongated beam in the VLA BnA configuration) differed by $0\farcs5$ in R.A. and $0\farcs2$ in decl. from the positions given in Hummel & Saikia (1991; observed at 6 cm with a $1\farcs2$ beam) and in Carral, Turner, & Ho (1990; observed at 2 cm with a $0\farcs2$ beam). Since the positions from the latter two observations agree very well with each other, while bridging our observations in frequency and resolution, we concluded that our position was in error and hence used the position of the radio nucleus given by Carral et al. (1990; see Table 3) for the radio/optical registration.

For those galaxies with ground-based optical positions of subarcsecond accuracy, the agreement between the radio and the optical frame should be better than $\sim 0\farcs4$ (see Fig. 1 in AE90). With the exception of NGC 7212, the radio and optical R.A.s and declinations do agree to within this accuracy (compare cols. [4], [5], [6], and [7] of Table 3). However, this is still not good enough, given the $\simeq 0\farcs1$ resolution of the *HST* images. To obtain an even better, though somewhat arbitrary, alignment, we applied a further shift for each galaxy, as discussed on a galaxy-by-galaxy basis below and in § 3.1. In general, we tried to identify the nucleus in our radio images (usually the blob closest to the nominal optical position) and then aligned the radio nucleus with the optical continuum peak. This, of course, leaves the inherent uncertainty as to whether the radio nucleus is properly identified and whether there might be an offset between the radio and optical nuclei due to, for example, obscuration. This issue can only be solved by accurate, absolute optical astrometry of field stars visible in the *HST* frames or by exact IR astrometry with large-format arrays.

For Mrk 34 and Mrk 573, we find that the central radio peak and the optical peak (derived from the astrometric measurements) agree to within $0\farcs3$, so we shifted the *HST* nucleus onto the radio position. However, in NGC 7212 and NGC 4388, the difference between the optical peak (in the astrometric frame) and the radio peak seems larger than the expected errors, so we did not perform a shift.

For the two objects that do not have optical positions of subarcsecond accuracy, we registered optical emission-line and radio images by their morphological similarity. Smoothing of radio and optical emission-line structures to the same resolution yields a relatively robust alignment to within $0\farcs3$ for ESO 428-G14 (cf. Falcke et al. 1996b). The registration of Mrk 1210 is even simpler, since both optical and radio images are basically point sources, which we assumed are coincident.

3. RESULTS

Our *HST* observations of ESO 428-G14 and Mrk 573 have been (or will be) presented elsewhere (Falcke et al. 1996b; Wilson, Falcke, & Simpson 1998), and we show here only their overlays on the new radio maps. Images of the remaining galaxies in our sample are shown in Figures 1–5. For each galaxy except Mrk 1210, we show the continuum-subtracted Hα + [N II] and [O III] images, the excitation map (i.e., the [O III] images divided by the Hα + [N II] image—both were clipped below their 3 σ noise levels prior to the division), and a red continuum image, either our own narrowband continuum image or, if available, a broadband snapshot image from the *HST* archive (from the snapshot survey of galaxies by Malkan, Grojian, & Tam 1998). The emission-line images of Mrk 1210 are dominated by a single nuclear peak, so the excitation map is omitted. We have compared our large-aperture fluxes with those obtained from ground-based observations as compiled in Mulchaey et al. (1994) and find general agreement to within 20%. Only for NGC 4388 is the discrepancy larger, an effect most likely due to the large size of its NLR. The fluxes of Hα + [N II] and [O III] λ5007 for two different aperture sizes are given in Table 4.

Our VLA radio maps are presented in Figures 6 and 7. Cross sections along the radio axis of our excitation maps, the Hα + [N II] images, and the radio maps for each source are given in Figures 8–10, and overlays of radio and emission-line maps are shown in Figures 11 and 12. In the following sections, we will discuss each of the galaxies

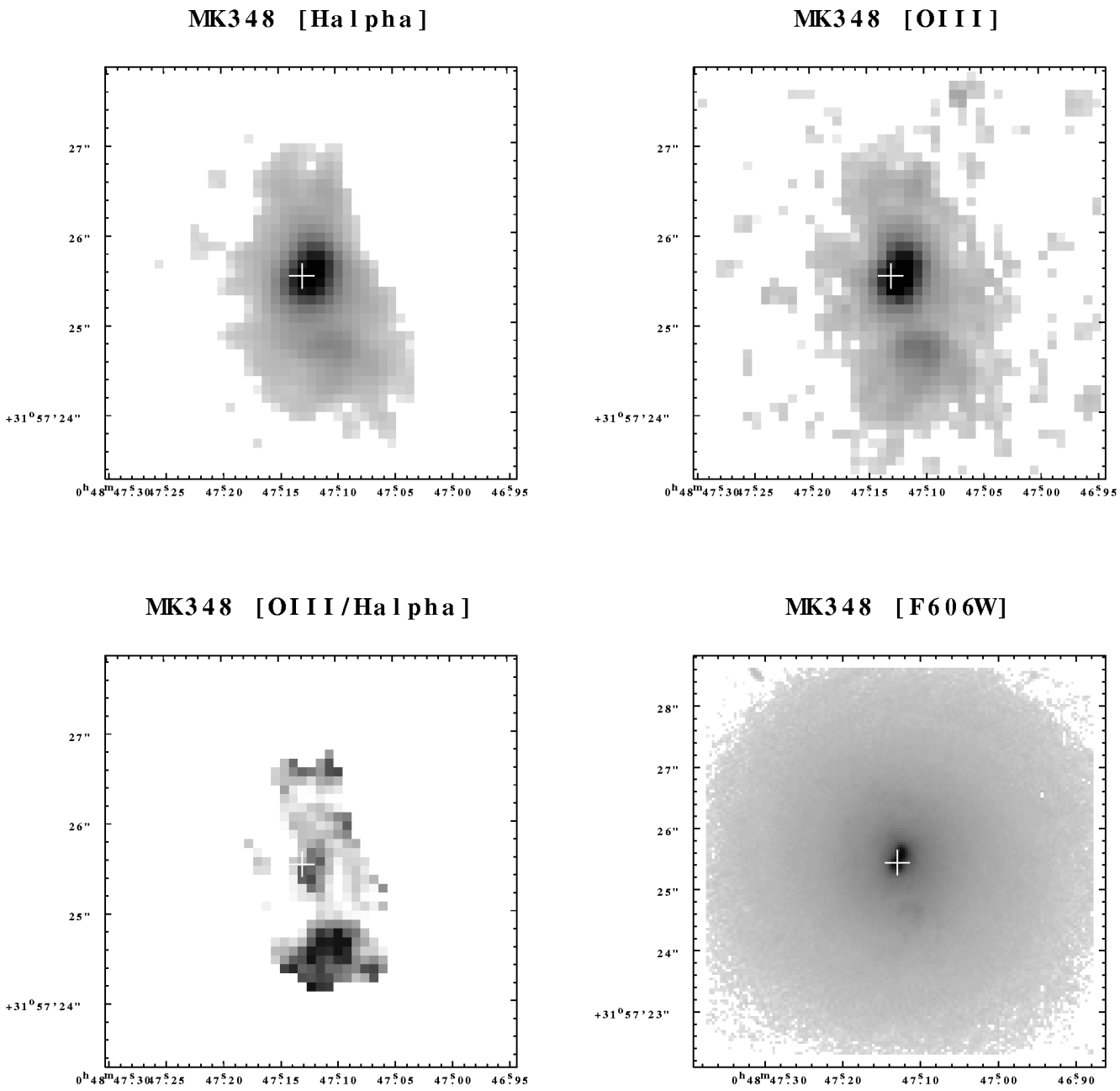

FIG. 1.—Mosaic of *HST* images for Mrk 348 with J2000 astrometric coordinates. North is up, east is to the left. *Upper left*, Hα + [N II]; *upper right*, [O III]; *lower left*, excitation map, darker shades correspond to higher [O III]-to-Hα + [N II] ratios; *lower right*, broadband continuum (F606W). White cross marks the red continuum peak.

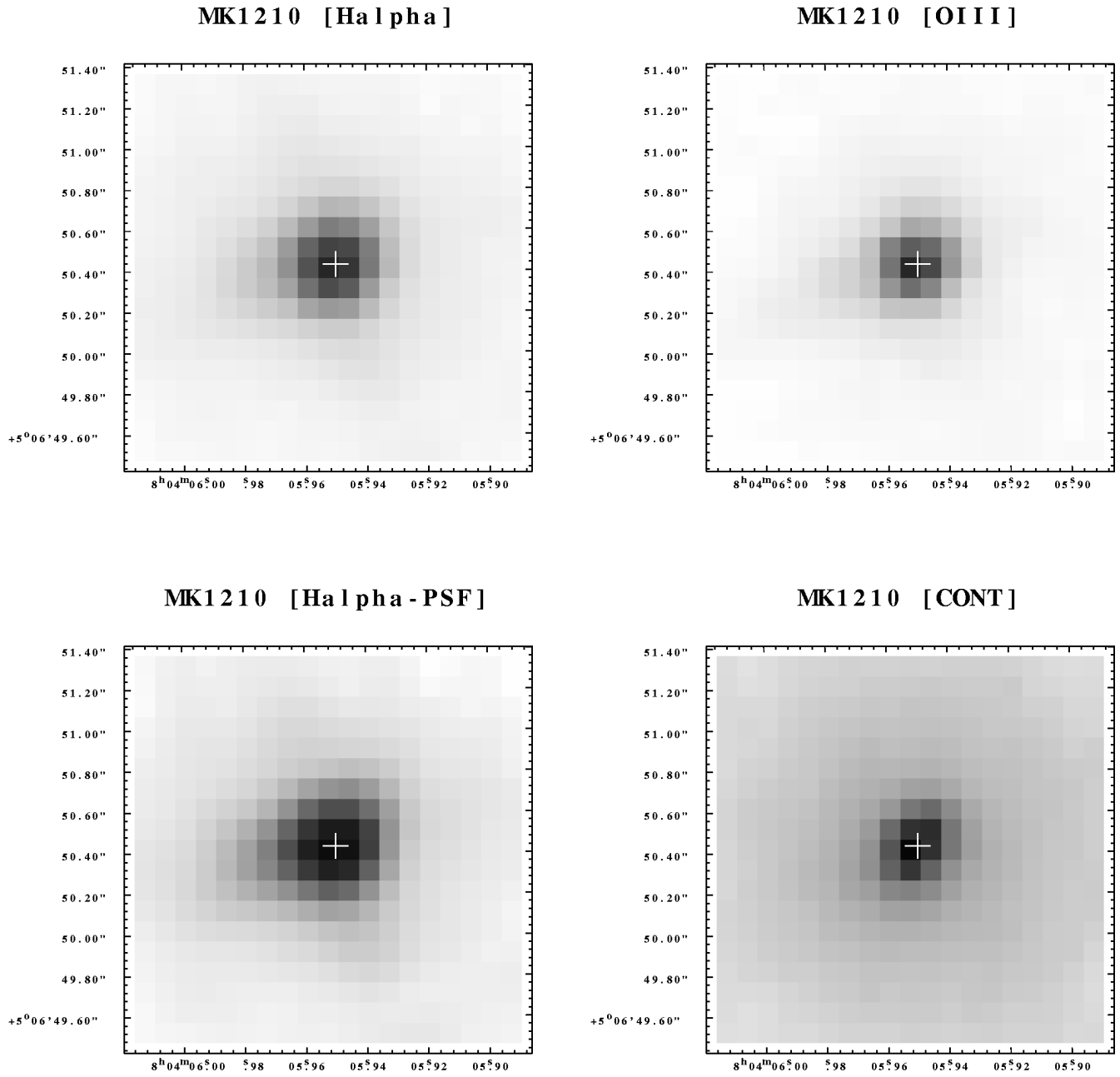

FIG. 2.—Mosaic of *HST* images for Mrk 1210 with J2000 coordinates. North is up, east is to the left. *Upper left*, Hα + [N II]; *upper right*, [O III]; *lower left*, PSF-subtracted Hα + [N II] image; *lower right*, red continuum image. White cross marks the red continuum peak.

individually. At the beginning of each paragraph we list the heliocentric redshift, the distance derived by converting the redshift to the Galactic standard of rest (de Vaucouleurs et al. 1991 [RC3]; NASA Extragalactic Database [NED]) and using Hubble's law (except for NGC 4388), and the linear scale corresponding to 0.″1, the typical pixel size.

3.1. *Comments on Individual Galaxies*

3.1.1. *Mrk 348*

Mrk 348 ($z = 0.01514$, $D = 62$ Mpc, $0.''1 \equiv 31$ pc) is a Seyfert 2 galaxy with a broad Hα emission line in polarized light (Miller & Goodrich 1990; Tran 1995). Mulchaey, Wilson, & Tsvetanov (1997) and Simpson et al. (1996) found a possible ionization cone in this galaxy, and Neff & de Bruyn (1983) discovered a triple radio source along P.A. 168° with an extent of 0.″2. This direction is approximately perpendicular to that of the optical polarization (P.A. 65°; Tran 1995). Capetti et al. (1996) observed this galaxy with the Faint Object Camera (FOC) on board the *HST* and resolved the [O III] emission-line gas in the inner arcsecond into a 0.″35-long feature at P.A. 155°. This feature can also be seen as an elongated nucleus in our lower resolution emission-line images and in the F606W broadband filter, which includes Hα and [N II] λλ6548, 6583 (Fig. 1). A similar, but less pronounced, elongation is indicated in both line-free continuum images in the inner 0.″3. Figures 1 and 8 and Table 4 show that the line emission is very concentrated within the central arcsecond. The excitation structure of the most extended gas of the NLR is difficult to interpret. The southern part could be described as triangular or fan-shaped, typical of ionization cones with an opening angle of

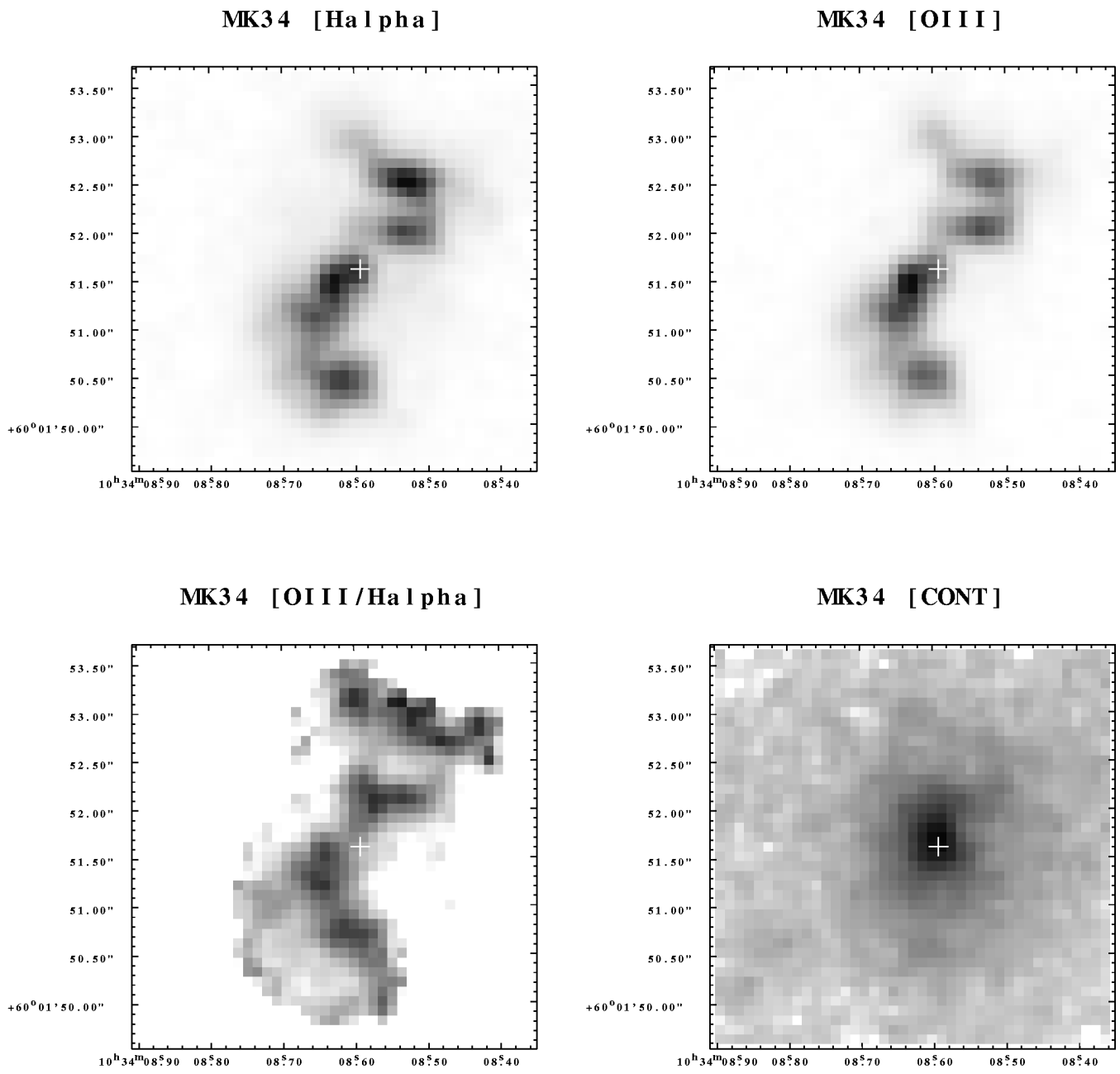

FIG. 3.—Mosaic of *HST* images for Mrk 34 with J2000 astrometric coordinates. North is up, east is to the left. *Upper left*, Hα + [N II]; *upper right*, [O III]; *lower left*, excitation map, darker shades correspond to higher [O III]-to-Hα + [N II] ratios; *lower right*, red continuum image. White cross marks the red continuum peak.

~90°. The structure is produced by the blob of highly excited gas 1″ south of the nucleus, also found by Capetti et al. (1996). Such a small-scale cone would be consistent with the southern ionization cone claimed by Mulchaey et al. (1997) and Simpson et al. (1996) on larger scales, but on the other hand it seems that the apex of this cone does not coincide with the optical nucleus. The good agreement between the VLBI radio and FOC optical structure (Capetti et al. 1996) suggests that the nuclear engine is indeed located near the optical nucleus, and in that case one would expect it to coincide with the apex of an ionization cone, even though the nominal position of the radio source given in Table 3 is in fact very close to the apex of the cone. Another problem, apart from the displacement of the cone's apex from the nucleus, is that the northern part of the emission-line gas does not exhibit anything resembling a fan shape. That could, however, be a result of obscuration or an inhomogeneous gas distribution.

3.1.2. *Mrk 573*

Mrk 573 ($z = 0.0173$, $D = 70$ Mpc, $0''.1 \equiv 34$ pc) is known from ground-based observations to have an extended emission-line region (e.g., Unger et al. 1987; Haniff et al. 1988; Tsvetanov & Walsh 1992) with a triple radio source (Ulvestad & Wilson 1984). Whittle et al. (1988) found kinematic substructure in the [O III] emission line at the position of the radio hot spots. High-resolution imaging of the NLR of Mrk 573 (Pogge & De Robertis 1995; Capetti et al. 1996) reveals a biconical excitation structure enveloping two sets of bow shock–like emission-line strands outside the

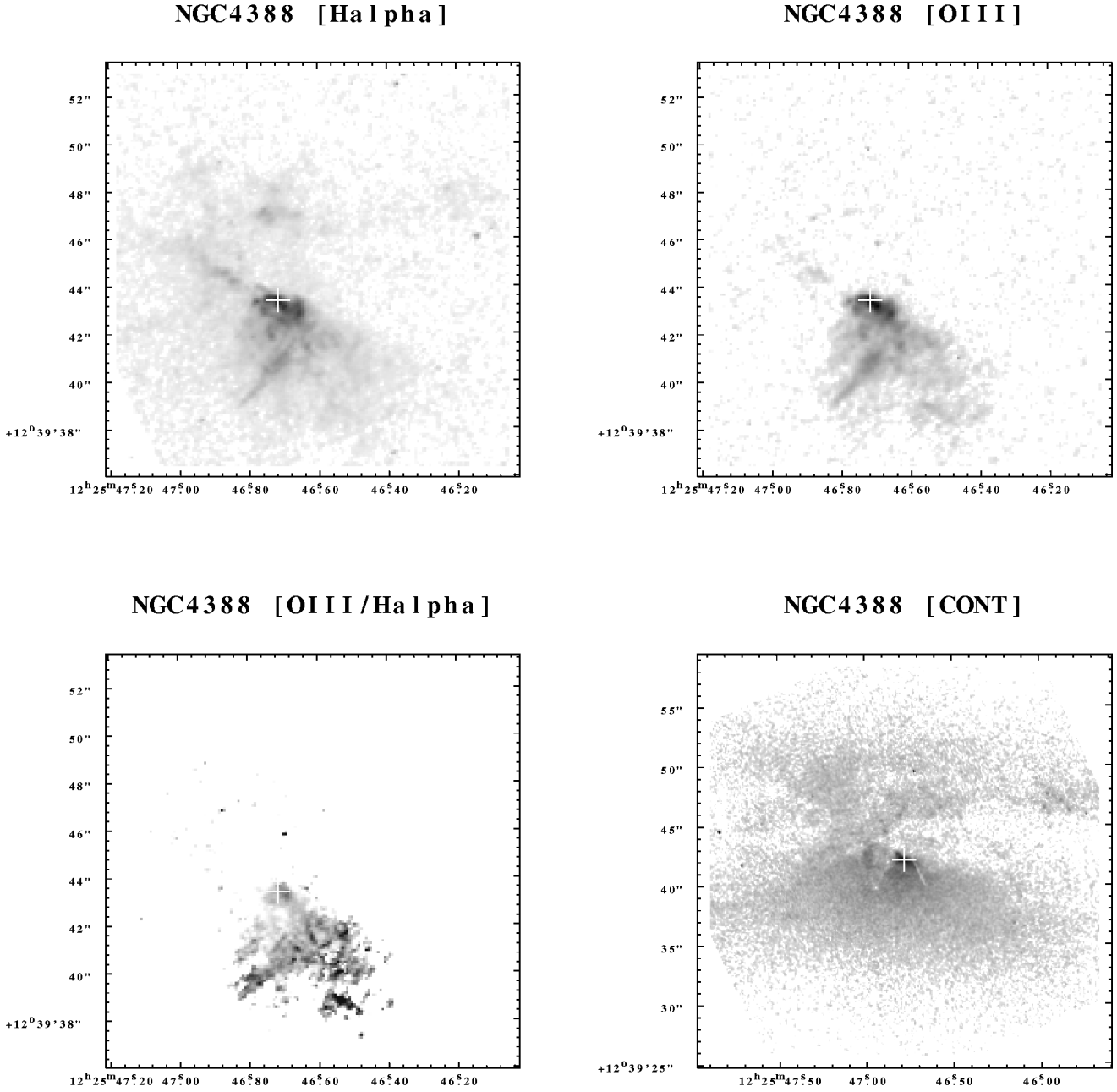

FIG. 4.—Same as Fig. 3, for NGC 4388

TABLE 4

HST EMISSION-LINE FLUXES

Galaxy (1)	Aperture 1 (arcsec) (2)	Hα + [N II] Flux (3)	[O III] λ5007 Flux (4)	Aperture 2 (arcsec) (5)	Hα + [N II] Flux (6)	[O III] λ5007 Flux (7)
Mrk 348	3	2.0	4.1	0.8	1.5	3.2
Mrk 573	10	7.1	14.3	1.0	1.5	3.5
ESO 428-G14	6	9.6	17.4	1.0	2.0	4.0
Mrk 1210	2	3.8	10.4	0.6	2.9	8.9
Mrk 34	4	3.6	6.1	1.0	0.7	1.3
NGC 4388	12	10.1	11.7	2.0	1.9	3.0
NGC 7212	6	4.5	9.3	0.8	1.7	3.9

NOTE—Fluxes given are in units of $\times 10^{-13}$ ergs s^{-1} cm^{-2}. Fluxes were derived by summing the flux in the *HST* images inside a circular aperture centered on the optical continuum nucleus. The apertures were chosen such that the first aperture includes most of the NLR visible in the *HST* images; the second aperture is intended to represent the nuclear region. Columns (2) and (5) give the diameter of the apertures in arcseconds; columns (3) and (4) give emission-line fluxes in the Hα + [N II] and [O III] λ5007 filters for the large aperture; columns (6) and (7) give emission-line fluxes in the Hα + [N II] and [O III] λ5007 filters for the small aperture.

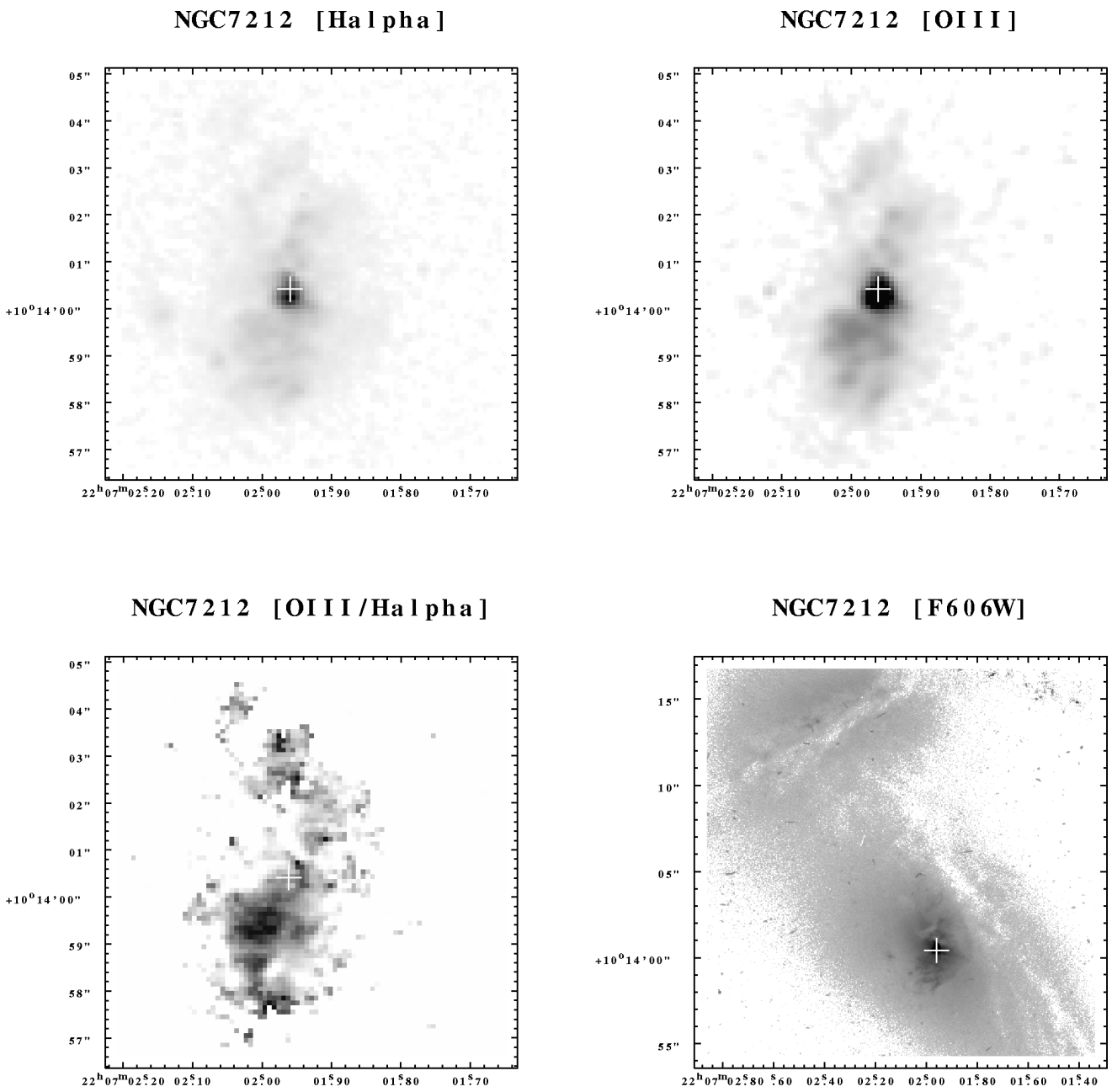

FIG. 5.—Same as Fig. 1, for NGC 7212

triple radio source (see Fig. 11). The emission-line structure will be discussed in more detail in Wilson et al. (1998). Here we present improved radio maps of this galaxy at 2 and 3.5 cm (Fig. 6). The 2 cm observations show structure in the three radio components for the first time. The central radio blob is elongated at P.A. $\sim 140°$ and has a shape similar to the emission-line structure associated with the optical peak.

This prompted us to align the peak in the radio emission with the optical continuum peak (Fig. 11). Pogge (1996) and Capetti et al. (1996), however, have argued that the real optical nucleus is hidden behind a dust lane, 0.″3 to the northwest. Both registrations are compatible with the astrometric positions to within the errors, so we cannot decide between them.

In the 3.5 cm map, the southeastern radio component is extended almost perpendicular to the source axis (Fig. 6), which may indicate that the plasma flow is redirected inside the bow shocks, as is also suggested by the 2 cm map. Comparison of the emission-line and the radio structure shows that the radio hot spots are located on the tips of two emission-line strands coming out of the nucleus, just inside the inner two emission-line arcs. In tapered, low-resolution 3.5 cm maps, we also find weak radio emission connecting the three blobs, and some very faint radio emission may be associated with the outer two emission-line arcs, some 2.″9 to the southeast and 3.″6 to the northwest of the nucleus. When comparing our highest resolution 3.5 cm map with a tapered 2 cm map, we find that the hot spots have steep radio spectra with α ($S_\nu \propto \nu^\alpha$) between -0.7 and -1 for the northwest hot spot and $\alpha \sim -0.5$ for the southeast hot spot. The central blob, however, has an inverted or flat spectrum ($\alpha \sim +0.2 \pm 0.2$), another clear indication that

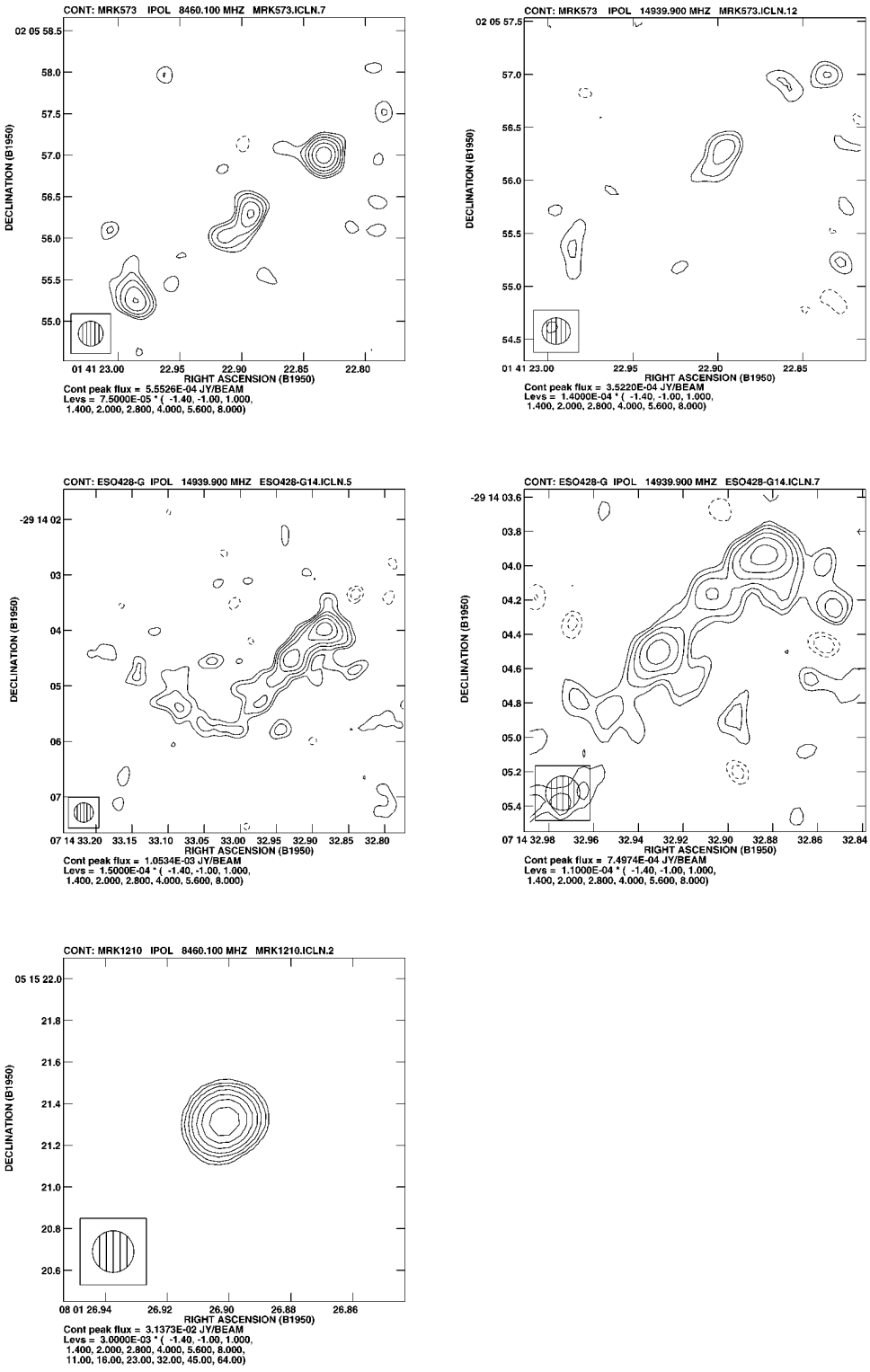

FIG. 6.—VLA maps with B1950 coordinates. North is up, east is to the left. *Upper left panel*: Mrk 573 at 3.5 cm with 0.″35 beam. The peak flux is 0.55 mJy (beam area)$^{-1}$, and contours are plotted at -1.4, -1 (*dotted line*), 1, 1.4, 2, 2.8, 4, and 5.6 times 0.075 mJy (beam area)$^{-1}$. *Upper right panel*: Mrk 573 at 2 cm with 0.″25 beam. The peak flux is 0.35 mJy (beam area)$^{-1}$, and contours are plotted at -1.4, -1 (*dotted line*), 1, 1.4, and 2 times 0.14 mJy (beam area)$^{-1}$. *Middle left panel*: ESO 428-G14 at 2 cm, tapered map with 0.″35 beam. The peak flux is 1.05 mJy (beam area)$^{-1}$, and contours are plotted at -1.4, -1 (*dotted line*), 1, 1.4, 2, 2.8, 4, and 5.6 times 0.15 mJy (beam area)$^{-1}$. *Middle right panel*: enlargement of ESO 428-G14 at 2 cm with 0.″2 beam. The peak flux is 0.75 mJy (beam area)$^{-1}$, and contours are plotted at -1.4, -1 (*dotted line*), 1, 1.4, 2, 2.8, 4, and 5.6 times 0.11 mJy (beam area)$^{-1}$. *Lower left panel*: Mrk 1210 at 3.5 cm with a 0.″2 beam. The peak flux is 31.4 mJy (beam area)$^{-1}$, and contours are plotted at -1.4, -1 (*dotted line*), 1, 1.4, 2, 2.8, 4, 5.6 and 8.0 times 3 mJy (beam area)$^{-1}$.

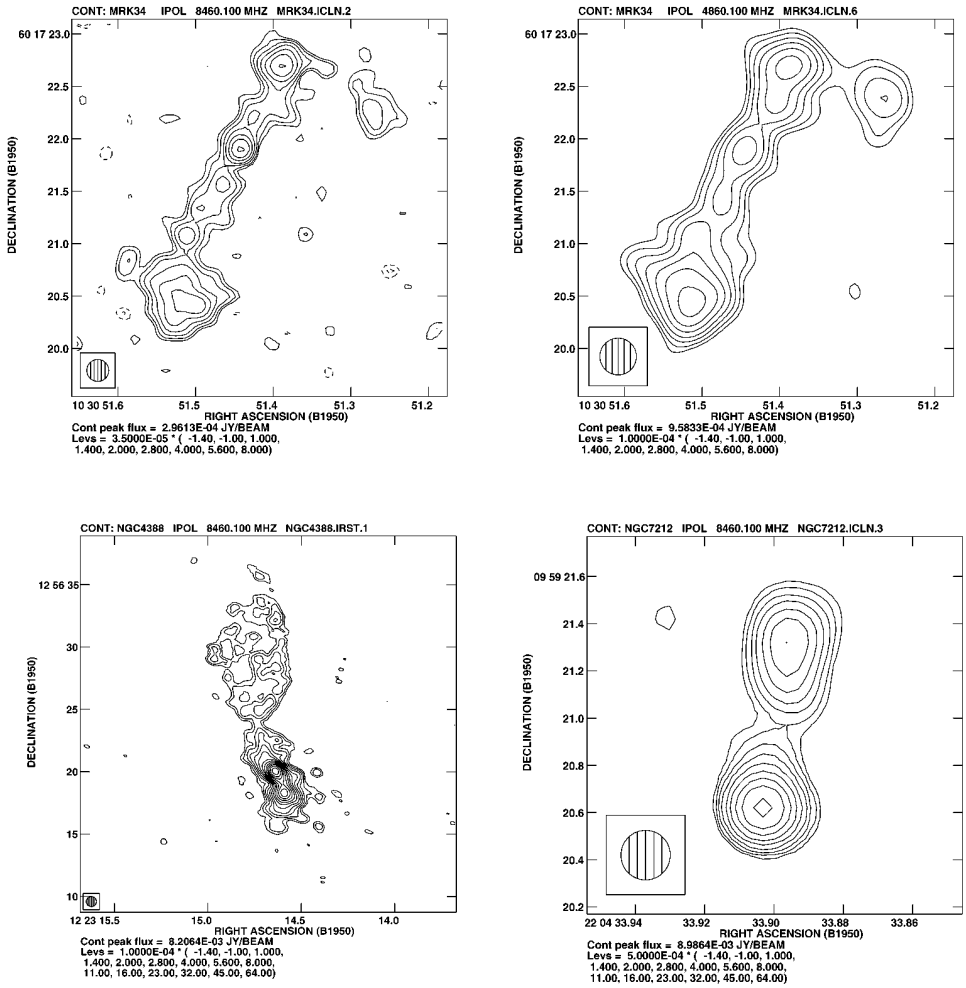

FIG. 7.—VLA maps with B1950 coordinates. North is up, east is to the left. *Upper left panel*: Mrk 34 at 3.5 cm with 0.″21 beam. The peak flux is 0.30 mJy (beam area)$^{-1}$, and contours are plotted at -1.4, -1 (*dotted line*), 1, 1.4, 2, 2.8, 4, 5.6 and 8.0 times 0.035 mJy (beam area)$^{-1}$. *Upper right panel*: Mrk 34 at 6.1 cm with 0.″35 beam. The peak flux is 0.96 mJy (beam area)$^{-1}$, and contours are plotted at -1.4, -1 (*dotted line*), 1, 1.4, 2, 2.8, 4, 5.6 and 8.0 times 0.1 mJy (beam area)$^{-1}$. *Lower left panel*: NGC 4388 at 3.5 cm with 0.″8 beam. The peak flux is 8.2 mJy (beam area)$^{-1}$, and contours are plotted at -1.4, -1 (*dotted line*), 1, 1.4, 2, 2.8, 4, 5.6, 8.0, 11.0, 16.0, 23.0, 32.0, 45.0, and 64.0 times 0.1 mJy (beam area)$^{-1}$. The coordinates for our map of NGC 4388 differ slightly from those of Hummel & Saikia (1991) and Carral et al. (1990) (see § 2.3). *Lower right panel*: NGC 7212 at 3.5 cm with 0.″21 beam. The peak flux is 9.0 mJy (beam area)$^{-1}$, and contours are plotted at -1.4, -1 (*dotted line*), 1, 1.4, 2, 2.8, 4, 5.6, 8.0, 11.0, and 16 times 0.5 mJy (beam area)$^{-1}$.

this is the radio nucleus. Figure 8 (*bottom panel*) also shows that the radio hot spots coincide with regions of reduced excitation.

3.1.3. *ESO 428-G14*

ESO 428-G14 ($z = 0.00544$, $D = 19.0$ Mpc, 0.″1 $\equiv$ 9.2 pc) was described in more detail in Falcke et al. (1996b), where we also discussed the optical-radio registration. The emission-line images presented there showed an unusual structure, consisting of thin strands of ionized gas that form a figure eight to the northwest of the nucleus. Our new radio maps (Fig. 6) substantially improve on the earlier radio map of Ulvestad & Wilson (1989) in both sensitivity and resolution. The higher resolution 2 cm map shows a narrow jet to the northwest of the nucleus, terminating in a hot spot that coincides with the location where the emission-line strands end (Fig. 11). The radio jet is unresolved perpendicular to its axis with a beam of 0.″2. In Falcke et al. (1996b), we speculated that the helical emission-line strands would wrap around a collimated radio jet, with the strands formed in the boundary layer between jet and ISM. Not only do we find this jet in the radio now, but the images also show that the maximum separation of the optical strands transverse to the jet axis ($\sim$0.″3, Fig. 11) is wider than the radio jet itself, lending support to the boundary-layer hypothesis. One problem, however, is the exact radio/optical registration for ESO 428-G14, since with the current alignment, the radio jet does not go right through the middle of the figure eight (see enlargement Fig. 12). A shift of the radio by 0.″15 to the south would solve this problem, but would also imply an offset between radio and optical nuclei. Until high-precision astrometry is available for this galaxy, the exact relation between radio and optical emission will remain somewhat uncertain.

Nevertheless, a few important observations can be made. At the northwest tip (0.″85 from the nucleus) of the jet, the radio emission is associated with the northern optical strand (Fig. 12), and the northwest radio hot spot is associated with a region of low emission-line excitation (Fig. 9 and Fig. 11). Near the northwest radio hot spot, both the

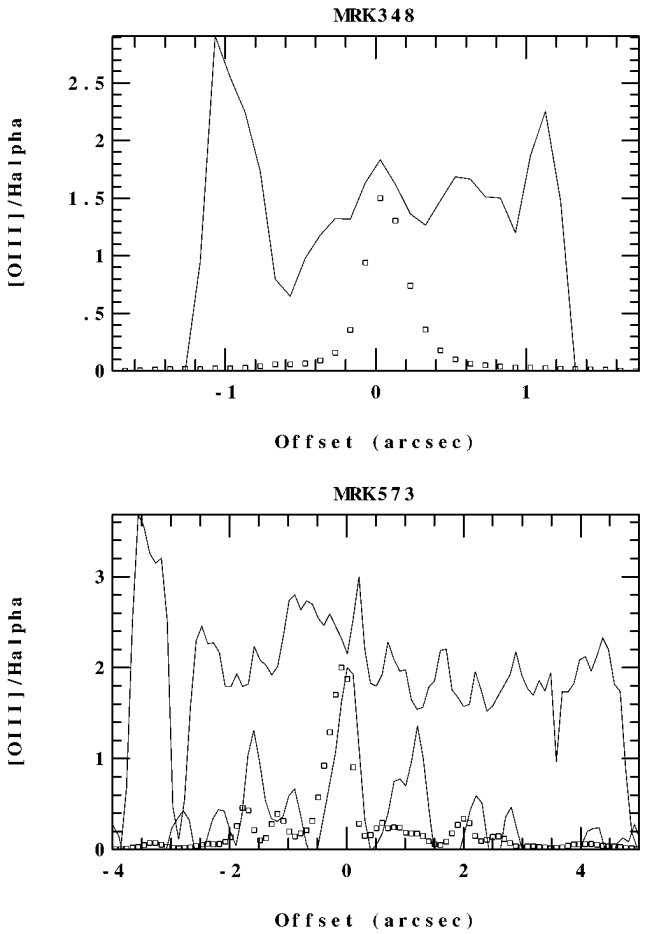

FIG. 8.—Three-pixel–wide cross sections along the position angle of the radio structure through the radio nucleus, which is at zero offset (north and northwest directions have positive offsets). *Top solid line*, [O III]/(Hα + [N II]) ratio; *boxes*, Hα + [N II] flux; *bottom solid line*, radio flux at the highest available frequency. The ordinate scale applies to both the [O III]/(Hα + [N II]) ratios and the Hα + [N II] brightnesses; the units for the latter are given below. *Top panel*: Mrk 348 at P.A. = 0° (no radio flux distribution); ordinate scale for the Hα + [N II] brightness is in units of 3.2×10^{-15} ergs s^{-1} cm^{-2} 0.″1^{-2}. *Bottom panel*: Mrk 573 at P.A. = −54° (2 cm map); ordinate scale for the Hα + [N II] brightness is in units of 2.95×10^{-15} ergs s^{-1} cm^{-2} 0.″1^{-2}.

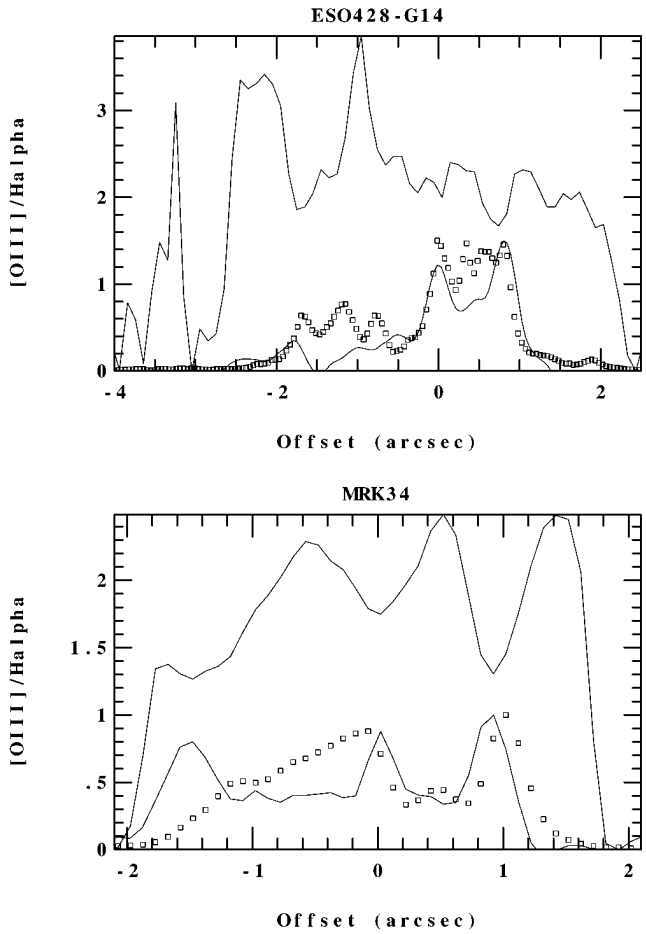

FIG. 9.—As Fig. 8. *Top panel*: ESO 428-G14 at P.A. = −46° (2 cm map); ordinate scale for the Hα + [N II] brightness is in units of 4.2×10^{-15} ergs s^{-1} cm^{-2} 0.″1^{-2}. *Bottom panel*: Mrk 34 at P.A. = −27° (3.5 cm map); ordinate scale for the Hα + [N II] brightness is in units of 2.0×10^{-15} ergs s^{-1} cm^{-2} 0.″1^{-2}.

radio jet and the optical strand bend toward the south for 0.″3 until they intersect the southern strand. Farther to the northwest, ∼1.″2 from the nucleus, we also find some radio emission that might be associated with the faint, linear, high-excitation [O III] feature sticking out of the figure eight toward the northwest.

The southeastern part of the radio jet has a lower surface brightness than the northwest structure, consisting of at least one faint strand that roughly follows, but is not coincident with, the optical strands (Fig. 6 and Fig. 11). There is some indication that at roughly the same distance from the nucleus as the northwest hot spots, the southeast radio jet splits into two, the northern jet being much fainter than the southern one. This northern jet is, in fact, more clearly visible on our 3.5 cm map (not shown here) and appears to be significant. Interestingly, the location where the jet splits coincides with the region of highest excitation in the ionized gas (Fig. 11). Toward the southeastern end, the radio jet clearly bends to the north, as does the high-excitation ionized gas.

3.1.4. *Mrk 1210*

Mrk 1210 ($z = 0.0135$, $D = 52$ Mpc, 0.″1 ≡ 25 pc) is another Seyfert 2 galaxy selected on the basis of its broad emission lines seen in polarized light (e.g., Tran 1995). The emission-line structure we find in this galaxy is the most compact in our whole sample. The emission is dominated by a single central peak (Fig. 2). We have compared radial profiles of the nuclear emission-line peak with those of stars in our FOV and could not find any significant differences. Hence, this compact, bright part of the nuclear line emission is <40 pc in extent.

We then tried to subtract the central point source to look for any faint, extended emission. This is a difficult task, since the point spread function (PSF) for the LRFs is a function of wavelength and position on the four chips, and will be different for each exposure. Unless one explicitly makes a separate PSF observation, it is almost impossible to find an exactly matching PSF in the archive. Hence, we composed an average PSF from five stars that were visible in the FOV of our Hα + [N II] image of Mrk 1210 and which had more than 1000 counts. The stars were shifted onto a common center, scaled and weighted according to their peak flux, and then coadded. Finally, we subtracted this average PSF image from the continuum-subtracted, but not rotated,

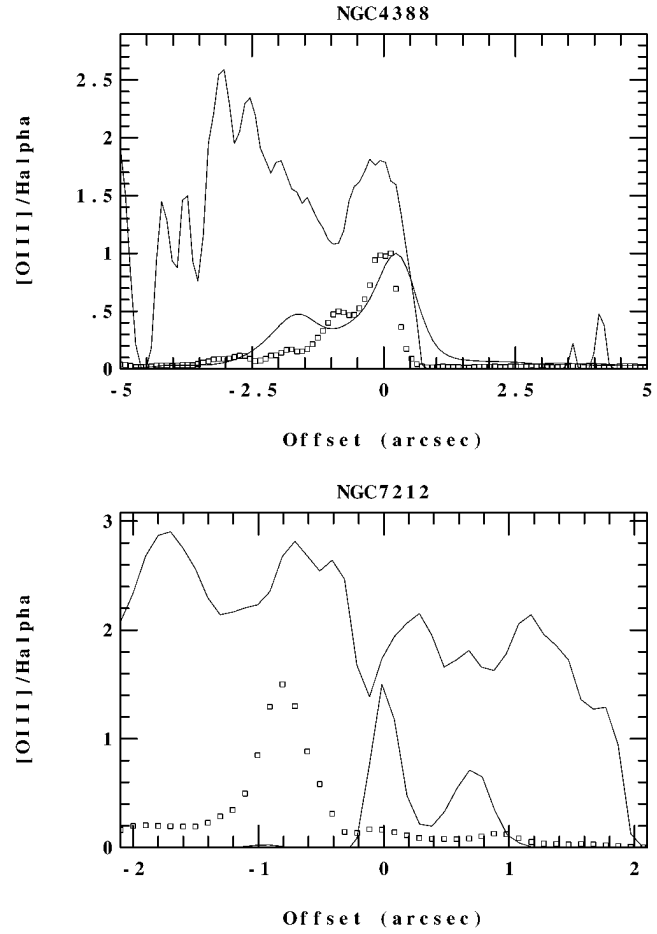

FIG. 10.—As Fig. 8. *Top panel*: NGC 4388 at P.A. = 24° (3.5 cm map); ordinate scale for the Hα + [N II] brightness is in units of 2.15×10^{-15} ergs s^{-1} cm^{-2} $0''.1^{-2}$. *Bottom panel*: NGC 7212 at P.A. = −7° (3.5 cm map); ordinate scale for the Hα + [N II] brightness is in units of 1.9×10^{-16} ergs s^{-1} cm^{-2} $0''.1^{-2}$ (Note: this cross section is significantly offset from the optical nucleus).

Hα + [N II] image of Mrk 1210 until the central pixel had the average flux value of its neighbors. The result is shown in Figure 2, in which the PSF-subtracted image has been rotated to the cardinal orientation. A PSF subtraction of the [O III] was not possible, since the FOV of this image did not include any stars with enough counts to determine the PSF reliably.

After subtraction the central point source, we find some faint, extended Hα + [N II] emission with a diameter of ∼0″.5 (Fig. 2). Some of the visible structure may, however, still reflect uncertainties in the PSF. If we divide the [O III] by the Hα + [N II] image (without PSF subtraction), we find an unusually high [O III] to Hα + [N II] ratio of 5 for the central peak, while the faint, extended emission has [O III]/(Hα + [N II]) ∼ 2 (determined in the region not dominated by the instrumental "spider" structure of the central peak).

Not surprisingly, the radio structure is also very compact, but is slightly resolved (Fig. 6). We find a total integrated flux of 39 mJy at 3.5 cm (31.4 mJy peak), which is consistent with earlier observations by Antonucci & Barvainis (1997 private communication), who obtained 39 mJy (total) at 3.5 cm and 16.3 mJy (total and peak) at the *K* band, thus yielding a spectral index of $\alpha = -0.7$ for the peak. This indicates a compact, nonvariable, steep-spectrum core. Parkes-Tidbinbilla interferometer (PTI) observations at 13 cm by Norris et al. (1990) found only 48 mJy, much less than the peak flux expected from extrapolation of the higher frequency observations (∼80 mJy). This difference could be due to either a low-frequency turnover, e.g., caused by free-free absorption, or resolution of the steep-spectrum core, even though the resolution of the PTI at 13 cm (∼0″.1) is not much higher than that of the VLA at 3.5 cm (∼0″.2).

Finally, we note that if the slight elongation to the southeast visible in the PSF-subtracted Hα + [N II] image (but see remarks above) and possibly also in the radio map is real, then this direction would be roughly perpendicular to the optical polarization vector (P.A. = 29°), as measured by Tran (1995). Only high-resolution radio mapping of this source, e.g., with the VLBA at lower frequencies, may be able to resolve this question and show whether there is an underlying jet structure in this source.

3.1.5. *Mrk 34*

Mrk 34 ($z = 0.0505$, $D = 205$ Mpc, 0″.1 = 100 pc) is the most distant and most luminous galaxy in our sample. Its [O III] luminosity of 3×10^{42} ergs s^{-1} is comparable to that of an average radio-quiet, low-redshift ($z < 0.5$) quasar in the Palomar-Green quasar sample (Boroson & Green 1992). From ground-based optical (Haniff et al. 1988) and VLA radio observations (Ulvestad & Wilson 1984), it is known that this galaxy has an extended structure, with two emission-line and radio lobes. Our emission-line images (Fig. 3) show an S-shaped structure resembling a sea horse. The inner part consists of one emission-line strand that seems to wiggle around a central axis along P.A. ≃ −37° until it terminates and bends through ∼90° at both ends. In the excitation map (Fig. 3), we find a bipolar high-excitation morphology, but the structures on opposite sides of the nucleus are not antiparallel, and the optical nucleus is offset from the apices of the structures. Obviously, the optical strand associated with the jet leaves its imprint in the excited gas, yielding an asymmetric appearence in the south.

Our radio maps also improve substantially upon earlier images. The maps show a radio jet with hot spots at each end (Fig. 7 and Fig. 11). The overall morphology is very straight along P.A. = −27°, with some small wiggles in the jet. This structure is unlike radio galaxies, since Mrk 34 has not only two pronounced hot spots, like luminous FR II radio galaxies, but also well defined, two-sided jets, as in low-luminosity FR I radio galaxies. The spectral indices we find for the jet from our X- and C-band data are extremely steep. The nuclear region has $\alpha \simeq -1$, and the northwest hotspot $\alpha \simeq -1.3$, while the spectrum of the southeast hotspot is even steeper, with $\alpha \simeq -1.7$. However, these numbers should be treated with caution, as resolution effects tend to steepen spectra taken in a single VLA configuration.

Since the astrometric positions (Table 3) indicate that the brightest peak in the jet is very close to the optical nucleus, we have aligned those two peaks. The emission-line structure then aligns very closely with the radio structure, so the ionized gas is physically associated with the radio jet (Fig. 11). Remarkably, the two radio hotspots coincide with pronounced regions of low excitation (Fig. 9 and Fig. 11; see also Fig. 3), possibly because the ionized gas is compressed to a higher density, so that the ionization parameter is reduced. Whittle et al. (1988) found that the gas associated

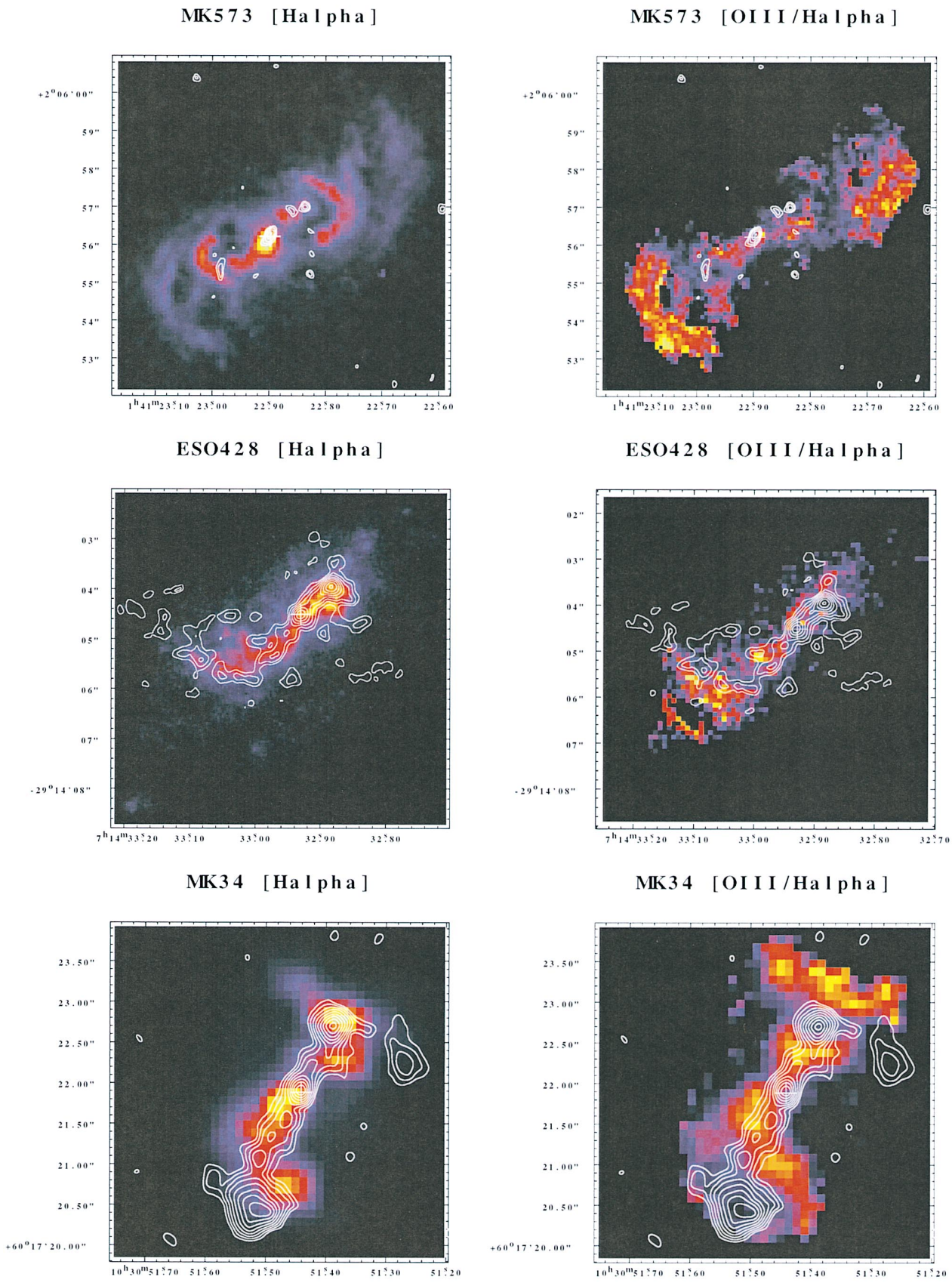

FIG. 11.—Hα + [N II] images and [O III]/(Hα + [N II]) excitation maps with radio contours overlaid. The coordinates are the B1950 coordinates of the radio maps. North is up, east is to the left. *Upper left*, Mrk 573, Hα + [N II], and 2 cm; *upper right*, Mrk 573, [O III]/(Hα + [N II]), and 2 cm; *middle left*, ESO 428-G14, Hα + [N II], and 2 cm; *middle right*, ESO 428-G14, [O III]/(Hα + [N II]), and 2 cm; *lower left*: Mrk 34, Hα + [N II], and 3.5 cm; *lower right*, Mrk 34, [O III]/(Hα + [N II]), and 3.5 cm.

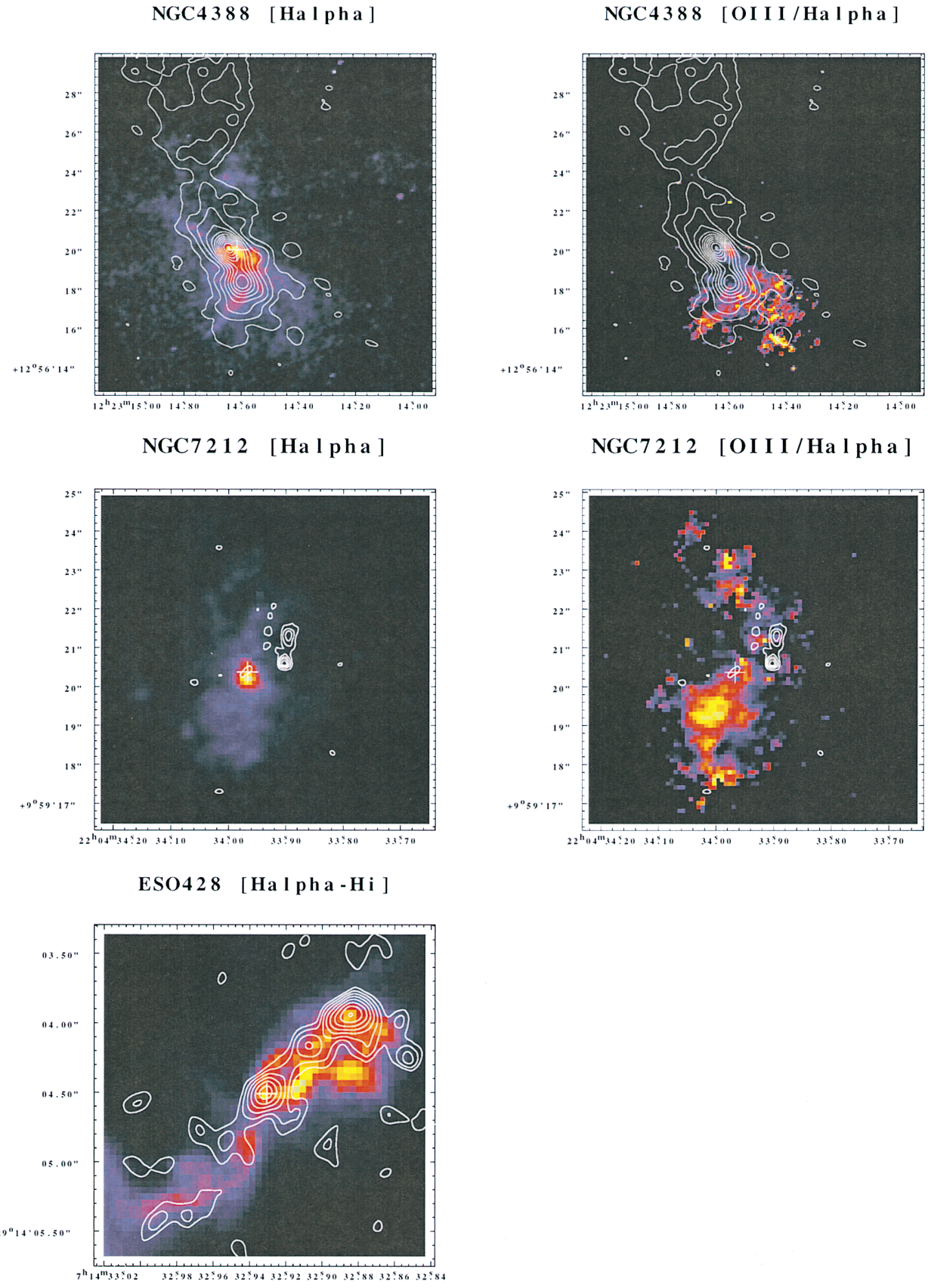

FIG. 12.—As Fig. 11. *Upper left*, NGC 4388, Hα + [N II], and 3.5 cm; *upper right*, NGC 4388, [O III]/(Hα + [N II]), and 3.5 cm; *middle left*, NGC 7212, Hα + [N II], and 3.5 cm; *middle right*, NGC 7212, [O III]/(Hα + [N II]), and 3.5 cm; *lower left*, enlargement of the figure-eight distribution of Hα + [N II] in ESO 428-G14 with the high-resolution 2 cm map overlaid. The radio coordinates for NGC 4388 are shifted to the frame of Carral et al. (1990).

with the radio hot spots has kinematically distinct properties and is clearly separated in velocity by several hundred km s^{-1} from the ambient gas.

3.1.6. *NGC 4388*

NGC 4388 ($z = 0.00842$, $D = 16$ Mpc, $0''.1 = 7.8$ pc) is assumed to be at the core of the Virgo cluster, for which we adopt a distance of 16 Mpc (van den Bergh 1996); thus, this galaxy is the closest in our sample. It is know from ground-based observations to have extended ionization cones (Pogge 1988; Corbin, Baldwin, & Wilson 1988).

The host galaxy is an edge-on spiral, and hence dust obscuration plays an important role in the interpretation of the optical structure. Our low-S/N continuum image (Fig. 4) shows two wedges of reduced emission, demonstrating the presence of obscuring dust bands along the disk of its galaxy right into the nuclear region. Several earlier papers have already suggested that NGC 4388 is an obscured Seyfert 1 galaxy on the basis of weak, broad Hα lines (Filippenko & Sargent 1985; see also Shields & Filippenko 1996), an inferred hidden ionizing continuum source (e.g., Colina 1992), and the presence of hard X-rays (Hanson et al. 1990). The velocity and excitation structure of the NLR is very complex (Corbin et al. 1988; Veilleux 1991) and might be described by rotation plus outflow. VLA maps have shown a central double source and a plume of radio plasma to the north of the optical nucleus (Stone, Wilson, & Ward 1988; Hummel & Saikia 1991).

Our Hα + [N II] image (Fig. 4) shows ionized gas extending $\sim 6''$ to the north and south of the nucleus. Both the [O III] image and the excitation map (Fig. 4) show a bright region of high-excitation gas to the south, including a very well defined ionization cone that is the exact continuation to smaller scales of the ionization cone found in ground-based images (e.g., Pogge 1988). A very interesting feature is a bright spike in the emission-line images, $2''.5$ south of the optical nucleus, that runs at a P.A. of 140° through the middle of the ionization cone.

Our 3.5 cm map of this galaxy (Fig. 7) confirms the structure found in earlier VLA observations, but shows more detail. The plume to the north is very pronounced and opens up dramatically after the radio outflow is tightly constricted ($4''$ to the north of the radio nucleus), resembling one half of a limb-brightened hour glass. The northern blob of the compact double source near the center of the galaxy appears to be the nucleus, since it has a flat spectrum down to at least 2 cm (see Carral et al. 1990).

As discussed in § 2.3, the exact alignment of radio and optical images of NGC 4388 requires care. Previous ground-based measurements of the optical nucleus (AE90) give a position almost $3''$ south of the radio nucleus. This is, however, an artifact resulting from the highly asymmetric emission-line region (Fig. 4) and the smoothing effect of atmospheric seeing. Our new registration (Fig. 12), using the nearby field star measured by Argyle (see § 2.3) and the radio position of the nucleus from Carral et al. (1990), shows that, in fact, the optical nucleus as seen with *HST* is within $0''.45$ of the radio nucleus and the apex of the ionization cone. The radio blob $2''$ to the south of the nucleus is clearly associated with the spike seen in the emission-line images, and this relationship is strongly suggestive of an interaction between the radio jet and a dense cloud in the ISM; faint radio emission also extends along this spike. We also note from the lowest radio contours that there seems to be low surface brightness radio emission filling the whole inner part of the ionization cone.

3.1.7. *NGC 7212*

NGC 7212 ($z = 0.0266$, $D = 110$ Mpc, $0''.1 = 53$ pc) is a Seyfert 2 galaxy in an interacting system of galaxies (Wasilewski 1981).[4] Both galaxies in the pair visible in our continuum image (Fig. 5) exhibit multiple dust lanes. The NLR structure is elongated and diffuse, with a strong central peak near the continuum peak and an overall structure resembling Mrk 348. The excitation map is more difficult to interpret, since there is no clear ionization cone visible, and the emission-line distribution in the north is partly obscured by the dust lanes. It might be said that the distribution of excitation to the south is consistent with a ragged ionization cone.

The VLA map of NGC 7212 (Fig. 7) shows a compact double source separated by $0''.7$ in the north-south direction, the northern blob being slightly elongated. The small angular extent in the radio is another point of similarity to Mrk 348.

Using the astrometry based on Argyle's star in the FOV of this galaxy, we find that the compact southern radio blob is offset by almost $1''$ to the northwest of the optical nucleus (Fig. 12). This is substantially larger than the typical errors in these astrometric observations and either indicates a not yet understood systematic error or is indeed significant. Our new position for the optical nucleus deviates by a few tenths of an arcsecond from the position given in Clements (1983), but the basic result remains the same for both positions, suggesting that the offset is real. Hence, this offset might indicate the presence of a strong dust lane in the nuclear region. Given our new position, the southern lobe of NGC 7212 seems to coincide with a low-excitation region (Fig. 12), an effect we have already seen in some of the other galaxies in our sample.

In general, we confirm the results of Tran (1995), who suggested that dust obscuration plays a significant role in this source (see also the broadband continuum image in Fig. 5) and found a jet extending up to $10''$ from the nucleus at P.A. = $-10°$ in ground-based [O III] and Hα images—exactly the same direction as the axis of the newly found double radio source on a much smaller spatial scale. As noted by Tran (1995), this direction is essentially perpendicular to that of the optical polarization (P.A. 93°), suggesting that the obscuring torus plus scattering region model may apply to NGC 7212.

4. DISCUSSION

We have observed a sample of seven Seyfert 2 galaxies with *HST* in the Hα + [N II] and [O III] emission lines and with the VLA at 3.5 cm and 2 cm to study the morphology of the NLR and its interaction with the radio outflows. We were able to resolve the NLR in six of the seven galaxies and in all cases found a very elongated emission-line region. In the four galaxies (Mrk 573, ESO 428-G14, Mrk 34, and NGC 4388) whose NLRs have the largest angular extent,

[4] Wasilewski classified this as a triple system. The component $40''$ southwest of the emission-line nucleus is not visible in the image shown here. On the archival F606W image, this component is much smaller than the two merging galaxies and highly elongated. In addition, the large FOV of the F606W image shows the rich structure and tidal tails created by the debris of this merger.

we find bipolar structures in excitation maps, which can be interpreted as either the ionization cones expected in the unified scheme or widening, self-excited matter outflows. In all cases where an ionization cone was known from ground-based observations (Mrk 573, NGC 4388, and possibly Mrk 348), we found an equivalent counterpart on the sub-arcsecond scale with a similar opening angle. This continuation and the straightness of the cone edges in NGC 4388 and Mrk 573 argue in favor of some kind of obscuring torus, with well-defined inner edges around the nucleus. Nevertheless, we find substantial structures within those cones that indicate that in the nuclear region, other processes (such as jet/ISM interactions) in addition to anisotropic radiation have a major impact on the excitation of the gas.

Our radio observations have resulted in high-quality maps of the galaxies in our sample, most of which show clear evidence for radio jets and/or lobes. Seyfert galaxies show a considerable diversity in their radio structures, with various morphologies: narrow jets (ESO 428-G14), triple structures with a core and two hot spots (Mrk 573), jets plus two hot spots (Mrk 34), radio plumes and limb-brightened lobes (NGC 4388), etc. This diversity suggests that Seyfert jets are much more influenced by jet-ISM interaction than FR I and FR II radio galaxies, which may not be surprising, since the radio power of Seyfert galaxies is orders of magnitudes smaller than in radio galaxies. The existence of this interaction is in fact well documented by the comparison between the radio continuum and emission-line images (Figs. 11 and 12). In those galaxies with polarized optical light (e.g., Tran 1995), we find that the polarization vector is perpendicular to the axis of the radio structure and the NLR (Mrk 348, NGC 7212, and possibly also in Mrk 1210). In several cases we also note that the excitation structure is influenced by the jet, e.g., radio hotspots seem to coincide with regions of reduced excitation (Mrk 573, Mrk 34, and probably also NGC 4388 and NGC 7212), while high-excitation regions are often found downstream of radio hotspots or regions where the jet bends or comes to an end (the southeast end of ESO 428-G14 and the southern hot spot of NGC 4388). It is obvious that not only is there a close correlation between the radio and the emission-line morphologies, but *the radio jet–ISM interaction is an important effect that strongly influences the excitation and morphology of the NLR.*

For example, the emission-line arcs in Mrk 573 wrap around the radio lobes. Our 2 cm maps (Fig. 6 and Fig. 11) also show that one of the radio lobes is elongated and bends in the region where the interaction is thought to occur. Furthermore, the reduced excitation (i.e., the [O III]/(Hα + [N II]) ratio) of the inner emission-line arcs is consistent with a lower ionization parameter, which can be understood if the arcs represent gas that has passed through a radiative bow shock, cooled, and increased in density. A similar effect is seen in Mrk 34, in which the radio lobes coincide with a low-excitation region, while the jet itself is surrounded by high-excitation gas. The wiggles seen in the radio jet of this galaxy could possibly be interpreted as some kind of Kelvin-Helmholtz instabilities between the radio plasma and the surrounding ionized gas.

ESO 428-G14 exhibits well-collimated, irregular emission-line strands on one side and a figure-eight morphology on the other. The latter has been interpreted as two helical emission-line strands wrapping around a radio jet (Falcke et al. 1996b). Our new, high-resolution maps indeed show a filamentary radio jet, which supports this idea; the northwest part of the radio jet is straight, with the emission-line helix possibly surrounding it, while the southeast radio jet splits into two at $\simeq 1''$ (90 pc) from the nucleus, again with a close relationship to the emission-line strands. However, since there is no possible registration in which the radio jet and the emission-line strands coincide precisely (there always seems to be a slight offset between those two structures), it seems likely that here too the emission-line gas wraps around the radio outflow.

Another example of an interaction between a radio jet and ambient gas is found in NGC 4388, where a bright spike is seen in the ionized gas at the end of the southern jet, while the radio plasma to the north flows apparently unhampered out of the galaxy disk and forms a large (~ 1 kpc) radio plume. Our 3.5 cm map also indicates that this radio plume may be hollow and hourglass-shaped. This structure is reminiscent of the radio lobe found, for example, in NGC 3079 (Seaquist, Davis, & Bignell 1978) and a few other galaxies (Ford et al. 1986). This kind of limb-brightened radio lobe stands in marked contrast to the well-collimated, stranded jets in ESO 428-G14 and NGC 4258 (e.g., Cecil, Wilson, & Tully 1992). An important difference is that NGC 3079 and NGC 4388 have jets that escape almost perpendicular to the galaxy plane, while in NGC 4258 and perhaps ESO 428-G14 the jet appears to be directed into the disk of the galaxy. The difference in radio morphology may then be ascribed to an external gas density that is much higher when the jet is in the disk than when it is in the galaxy halo.

Moreover, even the sources with compact NLRs support the jet-ISM interaction scenario, since all three such sources also have correspondingly compact radio structures. These sources happen to be those selected for *HST* observations on the basis of having hidden broad-line regions, visible in polarized light, rather than having extended emission lines in ground-based observations. The most extreme case of a compact NLR is Mrk 1210, in which the line emission is dominated by a point source (<40 pc) and which has the highest [O III]/(Hα + [N II]) ratio.

Hence, the most important conclusion to come out of this study is not only that an expectation of the unified scheme—ionization cones—is tentatively supported by the *HST* observations, but also that the influence of radio jets and their angle with respect to the galaxy plane cannot be ignored when discussing the structure, kinematics, and excitation of the NLR of Seyferts. Specifically, there seems to be a tendency for radio lobes to coincide with lower excitation regions, presumably as a result of the compression of the ambient gas.

As a consequence of this compression, one would also expect that compact regions with high emission-line brightnesses (e.g., the inner arcs in Mrk 573) would have high densities and thus low [O III]/Hα + [N II] ratios. Figure 13 shows diagrams in which we have plotted the emission-line brightness versus the [O III]/Hα + [N II] ratio for each pixel in the four images with the largest number of usable pixels (i.e., with emission-line brightness above the 3 σ noise level). The upper envelope for all these graphs has a characteristic peaked shape, indicating that the brightest features have only moderate excitation. In Mrk 573 and NGC 4388, the highest excitation is clearly found in the lowest brightness regions, as expected if variations in both of these

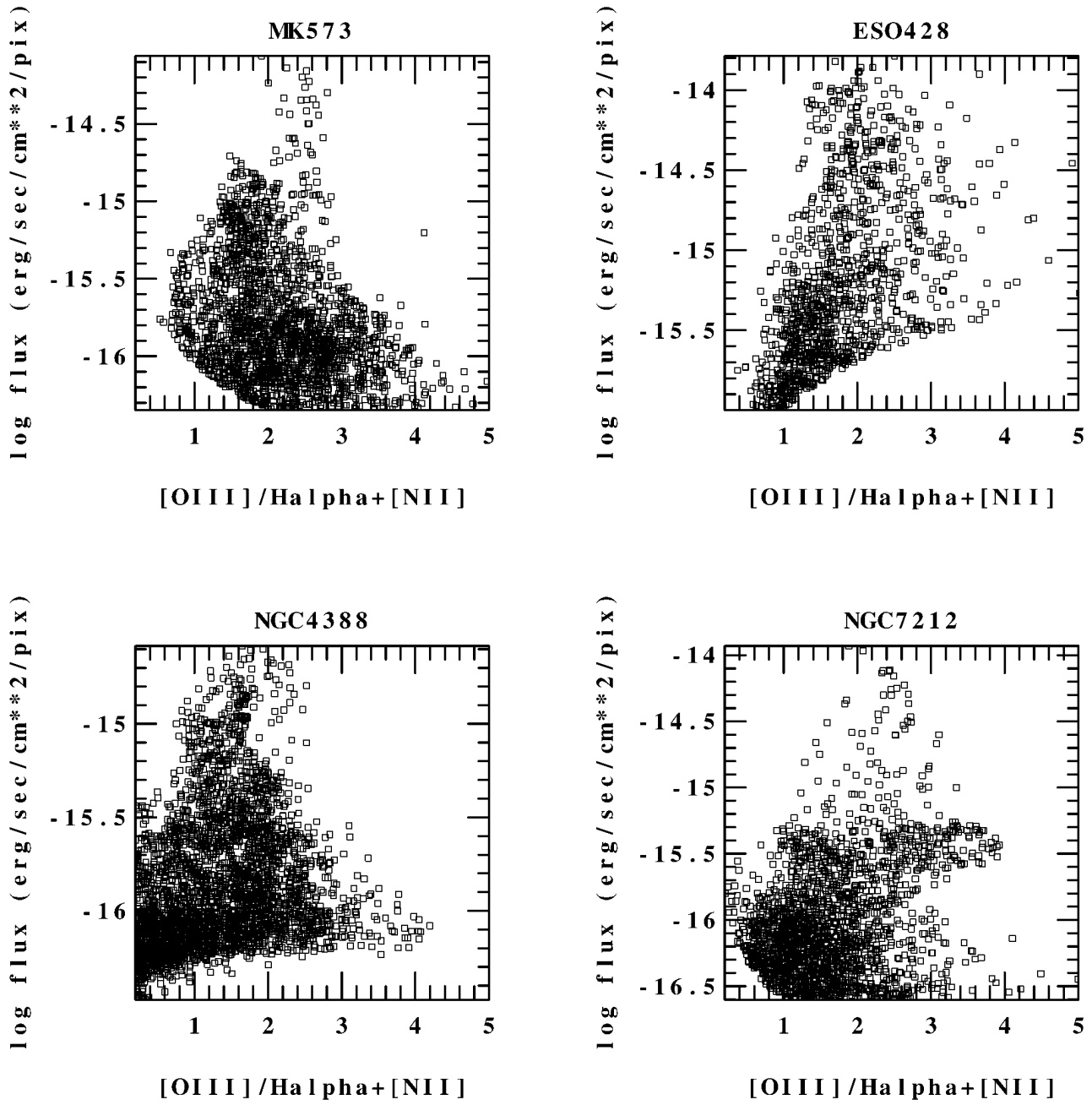

FIG. 13.—The four panels show the logarithm of the emission-line brightness versus the [O III]-to-Hα + [N II] ratio of each pixel in our images of Mrk 573 (*upper left*), ESO 428-G14 (*upper right*), NGC 4388 (*lower left*), and NGC 7212 (*lower right*). The fluxes per pixel for the ordinate were taken from the [O III] image for ESO 428-G14 (because Hα + [N II] was taken on the PC), and from the Hα + [N II] image for the rest.

parameters are primarily determined by variations in gas density. However, no such clear relationship is seen for ESO 428-G14 and NGC 7212. The detailed relation between line brightness and excitation will be influenced by other factors besides density, including the size of the cloud, the local intensity of the ionizing radiation, abundances, and whether the clouds are matter or ionization bounded. In addition, the inclusion of some of the [N II] $\lambda\lambda$6548, 6583 lines in our Hα images complicates the interpretation of these diagrams. It is thus not surprising that simple correlations are not seen in Figure 13.

Finally, it is interesting to consider the jets and NLR of Seyfert galaxies in the broader context of AGN physics. As pointed out before, some of our galaxies (e.g., Mrk 34 and Mrk 573) have [O III] luminosities comparable to radio-quiet, low-redshift quasars. For such objects, we are discussing a regime in which the quasar and Seyfert classifications overlap. One important feature of quasars is, however, that they come in two classes: radio-loud and radio-quiet. Using the well-known [O III] to radio correlations (e.g., Miller, Rawlings, & Saunders 1993; Falcke, Malkan, & Biermann 1995; Falcke 1996), it is clear that the Seyferts in our sample belong to the radio-quiet class of AGN, yet they not only show jets, but these jets are also kinematically important for the emission-line gas. The question of whether radio-quiet quasars also have jets has been debated for a while. Kellerman et al. (1994) found a number of radio-quiet quasars that have a double radio structure,

and Falcke, Patnaik, & Sherwood (1996a) found evidence for relativistic jets in radio-quiet quasars. The jets we find in Mrk 34 and Mrk 573 would in fact resemble some of the double structures seen by Kellerman et al. (1994) if placed at a larger distance and observed with lower sensitivity.

5. CONCLUSIONS

Our results have shown that observations of jets and NLRs in Seyfert galaxies allow a detailed look into the physics of the circumnuclear regions of AGN, with much better linear resolution than is possible for most of the more luminous AGN. Further studies of the NLR of Seyferts should take into account the fact that Seyfert jets leave their trace on the ISM. High (spatial)-resolution spectroscopy, such as is possible now with STIS on board the *HST*, should provide quantitative results for the kinematics, excitations, and densities involved in these jet-ISM interaction regions, and in this way give us important information not only on the kinematics of the NLR, but also on the kinematics and dynamics of low-power radio jets. Those observations may also settle the exact nature of the excitation of the NLR. Even though the radio jets substantially influence the NLR, it is still unclear whether the dominant source of ionizing photons is the compact, hidden Seyfert 1 nucleus or hot gas created in the jet-driven shocks.

We thank the STScI staff, J. Biretta, M. McMaster, and K. Rudloff for their support in the LRF calibrations. We are very grateful to R. W. Argyle (Royal Greenwich Observatory) for providing us with astrometric positions for the field stars near NGC 4388 and NGC 7212 prior to publication and to R. R. J. Antonucci for information on his VLA observations of Mrk 1210, made together with R. Barvainis. We also thank R. Pogge for refereeing the paper and the staff at NRAO in Socorro, especially J. S. Ulvestad, for their support. This research was supported by the Space Telescope Science Institute under grant GO5411, by NASA under grants NAGW-3268, NAGW4700, NAG8-1027, and in part by the DFG (Fa 358/1-1), and has made use of the NASA Extragalactic Database (NED), which is operated by Caltech/JPL. The National Radio Astronomy Observatory is a facility of the National Science Foundation, operated under a cooperative agreement by Associated Universities, Inc.

REFERENCES

Antonucci, R. R. J. 1993, ARA&A, 31, 473
Argyle, R. W., & Eldridge, P. 1990, MNRAS, 243, 504 (AE90)
Baldwin, J. A., Wilson, A. S., & Whittle, M. 1987, ApJ, 319, 84
Bicknell, G. V., Dopita, M. A., Tsvetanov, Z. I., & Sutherland, R. S. 1998, 495, 680
Boroson, T. A., & Green, R. F. 1992, ApJS, 80, 109
Bower, G. A., Wilson, A. S., Morse, J. A., Gelderman, R., Whittle, M., & Mulchaey, J. S. 1995, ApJ, 454, 106
Bower, G. A., Wilson, A. S., Mulchaey, J. S., Miley, G. K., Heckman, T. M., & Krolik, J. H. 1994, AJ, 107, 1686
Capetti, A., Axon, D. J., Macchetto, F., Sparks, W. B., & Boksenberg, A. 1996, ApJ, 469, 554
Capetti, A., Macchetto, F. D., Sparks, W. B., & Boksenberg, A. 1994, ApJ, 421,87
Carral, P., Turner, J. L., & Ho, P. T. P. 1990, ApJ, 362, 434
Cecil, G., Wilson, A. S., & Tully, R. B. 1992, ApJ, 390, 365
Clements, E. D. 1981, MNRAS, 197, 829
———. 1983, MNRAS, 204, 811
Colina, L. 1992, ApJ, 386, 59
Corbin, M. A., Baldwin, A. S., & Wilson, A. S. 1988, ApJ, 334, 584
de Bruyn, A. G., & Wilson, A. S. 1978, A&A, 64, 433
de Vaucouleurs, G., de Vaucouleurs, A., Corwin, H. G., Buta, R. J., Paturel, G., & Fouqué, P. 1991, Third Reference Catalogue of Bright Galaxies (New York: Springer)
Dopita, M. A. 1995, in STScI Symp. 8, The Analysis of Emission Lines, ed. R. E. Williams & M. Livio (Cambridge: Cambridge Univ. Press), 65
Dopita, M. A., & Sutherland, R. S. 1995, ApJ, 455, 468
Evans, I. N., Ford, H. C., Kinney, A. L., Antonucci, R. J., Armus, L., & Caganoff, S. 1991, ApJ, 369, L27
Falcke, H. 1996, in Jets from Stars and Galaxies, ed. W. Kundt (Berlin: Springer), 19
Falcke, H., Malkan, M., & Biermann, P. L. 1995, A&A, 298, 375
Falcke, H., Patnaik, A., & Sherwood, W. 1996a, ApJ, 473, L13
Falcke, H., Wilson, A. S., Simpson, C., & Bower, G. A. 1996b, ApJ, 470, L31
Filippenko, A. V., & Sargent, W. L. W. 1985, ApJS, 57, 503
Ford, H. C., Dahari, O., Jacoby, G. H., Crane, P., & Ciardullo, R. 1986, ApJ, 311, L7
Haniff, C. A., Wilson, A. S., & Ward, M. J. 1988, ApJ, 334, 104
Hanson, C. G., Skinner, G. K., Eyles, C. J., & Willmore, A. P. 1990, MNRAS, 242, 262
Hummel, E., & Saikia, D. J. 1991, A&A, 249, 43
Kellermann, K. I., Sramek, R., Schmidt, M., Green, R., & Shaffer, D. B. 1994, AJ, 108, 1163
Kojoian, G., Elliot, R., & Bicay, M. D. 1981, AJ, 86, 816
Malkan, M. A., Grojian, F., & Tam, R. 1998, ApJS, submitted
Miller, J. S., & Goodrich, R. W. 1990, ApJ, 335, 456
Miller, P., Rawlings, S., & Saunders, R. 1993, MNRAS, 263, 425
Morse, J. A., Raymond, J. C., & Wilson, A. S. 1996, PASP, 108, 426
Mulchaey, J. S., Wilson, A. S., Bower, G. A., Heckman, T. M., Krolik, J. H., & Miley, G. K. 1994, ApJ, 433, 625
Mulchaey, J. S., Wilson, A. S., & Tsvetanov, Z. 1997, ApJS, 102, 309
Neff, S. G., & de Bruyn, A. G. 1983, A&A, 128, 318
Norris, R. P., Allen, D. A., Sramek, R. A., Kesteven, M. J., & Troup, E. R. 1990, ApJ, 359, 291
Pogge, R. W. 1988, ApJ, 332, 702
———. 1996, in ASP Conf. Ser. 113, Emission Lines in Active Galaxies: New Methods and Techniques, ed. B. M. Peterson, F.-Z. Cheng, & A. S. Wilson (San Francisco: ASP), 378
Pogge, R. W., & De Robertis, M. M. 1995, ApJ, 451, 585
Seaquist, E. R., Davis, L., & Bignell, R. C. 1978, A&A, 63, 199
Shields, J. C., & Filippenko, A. V. 1996, A&A, 311, 393
Simpson, C., Mulchaey, J. S., Wilson, A. S., Ward, M. J., & Alonso-Herrero, A. 1996, ApJ, 457, L19
Simpson, C., Wilson, A. S., Bower, G., Heckam, T., Krolik, J. H., & Miley, G. K. 1997, ApJ, 474, 121
Stone, J. L., Wilson, A. S., & Ward, M. J. 1988, ApJ, 330, 105
Storchi-Bergmann, T., Mulchaey, J. S., & Wilson, A. S. 1992, ApJ, 395, L73
Tran, H. D. 1995, ApJ, 440, 578
Tsvetanov, Z., & Walsh, J. R. 1992, ApJ, 386, 485
Ulvestad, J. S., & Wilson, A. S. 1984, ApJ, 278, 544
———. 1989, ApJ, 343, 659
Unger, S. W., Pedlar, A., Axon, D. J., Whittle, M., Meurs, E. J. A., & Ward, M. J. 1987, MNRAS, 228, 671
van den Bergh, S. 1996, PASP, 108, 109
Veilleux, S. 1991, ApJ, 369, 331
Véron-Cetty, M. P., & Véron, P. 1996, ESO Sci. Rep. 17, 1-276
Wasilewski, A. J. 1981, PASP, 93, 560
Whittle, M. 1985, MNRAS, 213, 33
———. 1992, ApJ, 387, 109
Whittle, M., Pedlar, A., Meurs, E. J. A., Unger, S. W., Axon, D. J., & Ward, M. J. 1988, ApJ, 326, 125
Wilson, A. S. 1996, in ASP Conf. Ser. 113, Emission Lines in Active Galaxies: New Methods and Techniques, ed. B. M. Peterson, F.-Z. Cheng, & A. S. Wilson (San Francisco: ASP), 246
Wilson, A. S., Braatz, J. A., Heckman, T. M., Krolik, J. H., & Miley, G. K. 1993, ApJ, 416, L61
Wilson, A. S., Falcke, H., & Simpson, C. 1998, in preparation
Wilson, A. S., & Willis, A. G. 1980, ApJ, 240, 429

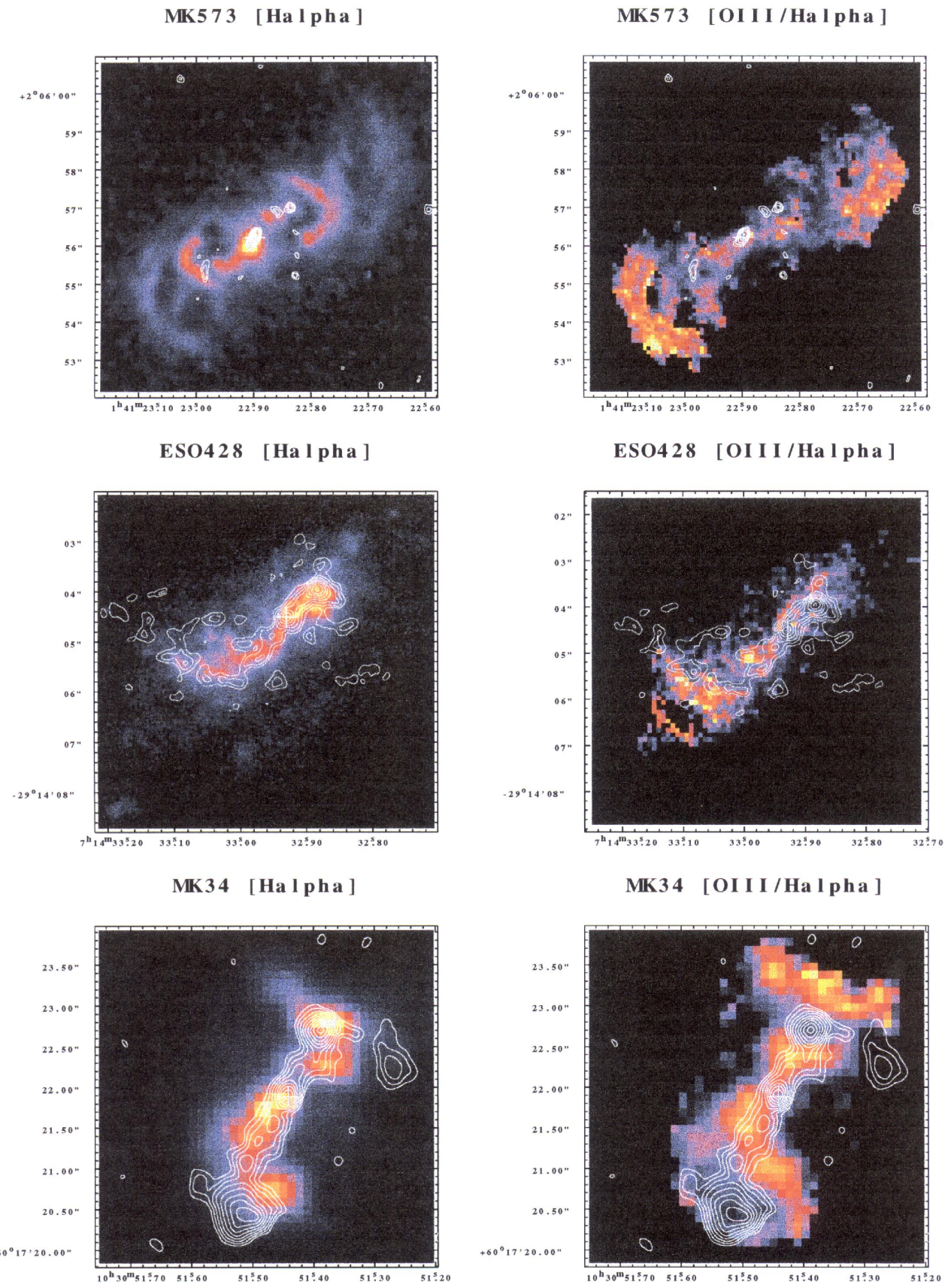

FIG. 11.—Hα + [N II] images and [O III]/(Hα + [N II]) excitation maps with radio contours overlaid. The coordinates are the B1950 coordinates of the radio maps. North is up, east is to the left. *Upper left*, Mrk 573, Hα + [N II], and 2 cm; *upper right*, Mrk 573, [O III]/(Hα + [N II]), and 2 cm; *middle left*, ESO 428-G14, Hα + [N II], and 2 cm; *middle right*, ESO 428-G14, [O III]/(Hα + [N II]), and 2 cm; *lower left*: Mrk 34, Hα + [N II], and 3.5 cm; *lower right*, Mrk 34, [O III]/(Hα + [N II]), and 3.5 cm.

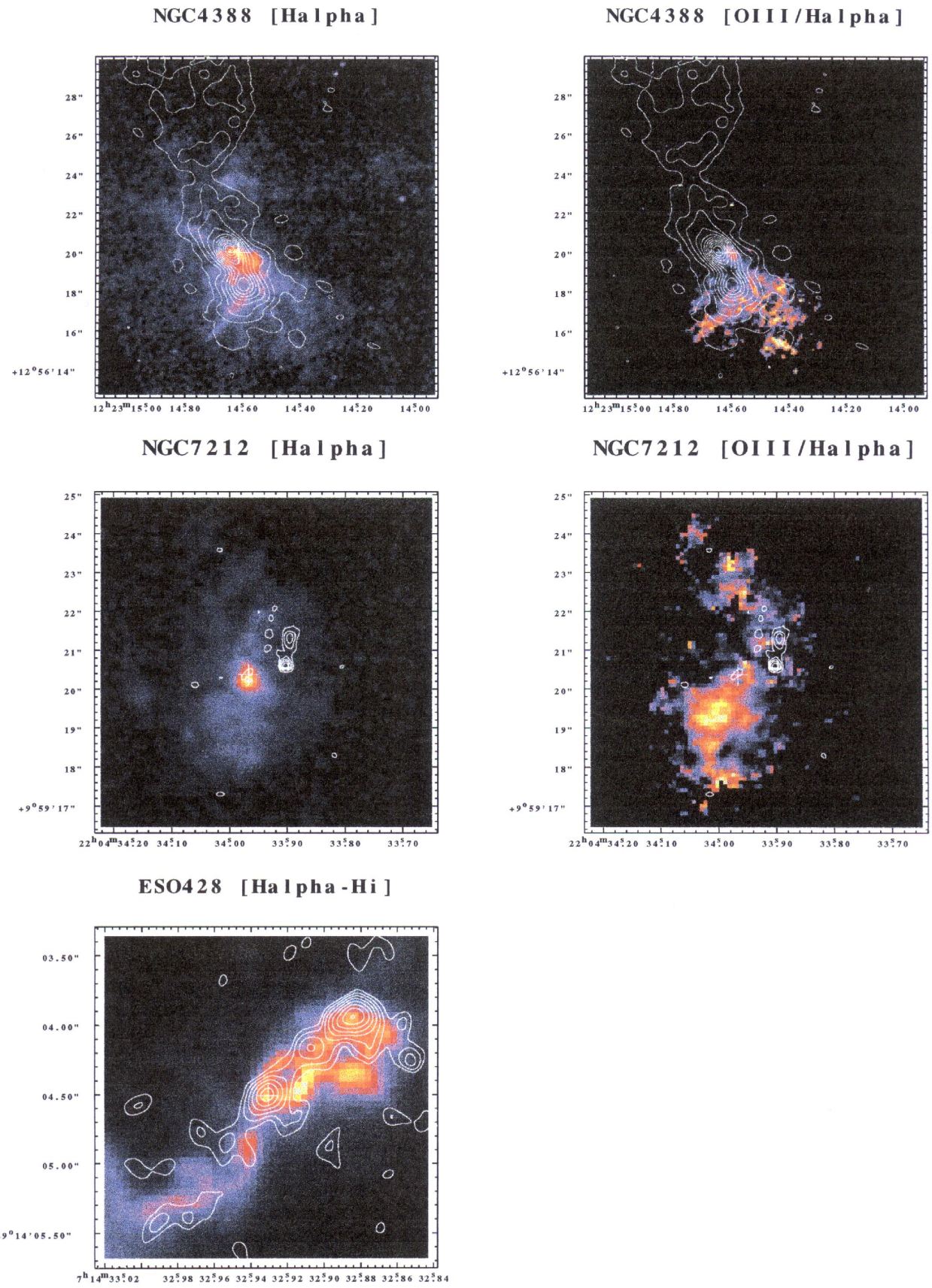

FIG. 12.—As Fig. 11 [Pl. 000]. *Upper left*, NGC 4388, Hα + [N II], and 3.5 cm; *upper right*, NGC 4388, [O III]/(Hα + [N II]), and 3.5 cm; *middle left*, NGC 7212, Hα + [N II], and 3.5 cm; *middle right*, NGC 7212, [O III]/(Hα + [N II]), and 3.5 cm; *lower left*, enlargement of the figure-eight distribution of Hα + [N II] in ESO 428-G14 with the high-resolution 2 cm map overlaid. The radio coordinates for NGC 4388 are shifted to the frame of Carral et al. (1990).